Amyloid-beta precursor protein contributes to brain aging and learning decline

Dennis E.M. de Bakker[a,b,c,d], Mihaela Mihaljević[b], Kunal Gharat[a], Yasmin Richter[e], Sara Bagnoli[f], Frauke van Bebber[g], Lisa Adam[a], Farzana Shamim-Schulze[a], Oliver Ohlenschläger[a], Martin Bens[a], Emilio Cirri[a], Adam Antebi[b,h], Ivan Matić[b,h], Anja Schneider[i], Bettina Schmid[g], Alessandro Cellerino[a,f], Janine Kirstein[a,e], Dario Riccardo Valenzano[a,b,c,d,*]

[a]Leibniz Institute on Aging – Fritz Lipmann Institute (FLI), Beutenbergstrasse 11, 07745, Jena, Germany;

[b]Max Planck Institute for Biology of Ageing, Joseph-Stelzmann-Straße 9B, 50931 Cologne, Germany;

[c]Cluster of Excellence "Balance of the Microverse", Friedrich-Schiller-University, Jena, Germany;

[d]Jena University Hospital/Friedrich-Schiller-University, Jena, Germany.

[e]Friedrich-Schiller-University, Institute for Biochemistry and Biophysics, Hans-Knöll-Str. 2, 07745, Jena, Germany

[f]Scuola Normale Superiore, Piazza dei Cavalieri, 7, 56126 Pisa PI, Italy;

[g]German Center for Neurodegenerative Diseases Munich, Feodor-Lynen-Str. 17, 81377, München, Germany;

[h]Cologne Excellence Cluster on Cellular Stress Responses in Aging-Associated Diseases (CECAD); University of Cologne, 50931, Cologne, Germany;

[i]German Center for Neurodegenerative Diseases, Venusberg-Campus 1/99, 53127 Bonn, Germany;

*corresponding author: dvalenzano@leibniz-fli.de

Abstract

Brain aging is a key risk factor for many neurodegenerative diseases, yet its molecular and cellular mechanisms remain elusive. Amyloid-beta precursor protein (APP) is among the most studied proteins linked to brain pathology; however, its role in non-pathological brain aging remains poorly characterized. Here, we investigate the natural impact of APP on normal brain aging using the short-lived turquoise killifish (*Nothobranchius furzeri*), which exhibits rapid and spontaneous age-related decline. We found that a pyroglutamated APP derivative (APP_{pE11}) accumulates intra-neuronally in an age-dependent manner, co-localizing with a marker of cell death. We found that intraneuronal APP_{pE11} is also present in brains from healthy elderly humans, suggesting deep evolutionary conservation. To determine APP's role in spontaneous brain aging, we knock-out "amyloid precursor protein a" (*appa*) in killifish via CRISPR/Cas9. The lack of *appa* mitigated brain aging from a proteome-wide perspective, reduced age-related cell death and inflammation, and improved neuronal activity and learning capacity in aged individuals. Our findings show an ancestral and previously unrecognized role of amyloid-beta precursor protein in non-pathological brain aging, making it an ideal target for anti-aging interventions.

53 **Introduction**

54

55 The aging brain undergoes several changes, including increased protein aggregation, inflammation, and
56 neuronal degeneration, which is associated with a decline in cognitive capacity. These changes are often
57 exacerbated during neurodegenerative diseases, which possibly represent alternative aging trajectories[1–3].
58 Amyloid-beta precursor protein (APP) and its derivatives, including amyloid beta ($A\beta_{1-42}$) are highly
59 studied peptides that aggregate in the brain of normal – i.e., non-pathological – aging individuals as well
60 as Alzheimer's disease (AD) patients[4,5]. Genetic and pharmacological induction of $A\beta_{1-42}$ can drive
61 neurodegenerative symptoms in worms[6,7], flies[8,9] and mice[10–12], and monoclonal antibodies and
62 vaccination strategies targeting $A\beta_{1-42}$ are being developed to slow down cognitive decline in AD
63 patients[13–18]. However, whether APP derivatives play a key role in normal aging and whether they can be
64 targeted to reduce the degenerative brain phenotypes of the normal aging brain remains largely
65 unexplored.

66

67 The investigation of the effect of spontaneous accumulation of APP and its derivatives during aging
68 requires an animal model whose natural aging trajectory includes both APP(-derivative) accumulation, as
69 well as neurodegenerative phenotypes. Therefore, we set out to investigate the APP dynamics in a
70 naturally short-lived vertebrate, which displays robust brain aging phenotypes, the turquoise killifish
71 (*Nothobranchius furzeri*)[3]. Turquoise killifish have a median lifespan ranging from three to eight months
72 and rapidly develop a range of age-related phenotypes overlapping with human aging. These phenotypes
73 include sarcopenia[19], cancer susceptibility[20], telomere attrition[21,22], impaired regenerative capacity[23,24], as
74 well as a decrease in antibody diversity and increased immunosenescence[25–27]. Meanwhile, the killifish
75 brain is subjected to age-related protein aggregation[28–33], astrogliosis[34,35], inflammation[24,28,35,36], neuronal
76 degeneration[29,37–39] and reduced neurogenic potential[24,34,35], which together might underlie a decreased
77 learning capacity[39–41]. Since several brain aging phenotypes arise spontaneously, the turquoise killifish

78 has been proposed as a promising model to study spontaneous age-dependent neurodegenerative
79 processes [3,42].
80
81 Here, we investigate the role of amyloid-beta precursor protein (APP) in normal brain aging. Using
82 transcriptomics, proteomics, and immunohistochemistry, we show that with age, the killifish brain
83 becomes subjected to a robust inflammatory state accompanied by intracellular accumulation of a
84 pyroglutamated APP-derivative, a post-translational modification associated with increased toxicity[43,44].
85 Finally, we show that knocking out the *appa* isoform of the amyloid-beta precursor genes mitigates age-
86 related brain phenotypes.
87
88
89
90
91
92
93
94
95
96

Results

Amyloid-beta precursor protein is evolutionary conserved between humans and turquoise killifish and is expressed in the aged turquoise killifish brain

The turquoise killifish is a naturally short-lived species, reaching sexual maturity within 3 to 5 weeks post-hatching. In this study, we define killifish (strain ZMZ1001) as "young," "aged," and "old" based on their ages of 6 weeks, 6 months, and 9 months, respectively. These age categories correspond to survival rates of 100%, 89%, and 44% (**Figure 1a**). Old individuals display several visually apparent aging phenotypes, including spine curvature, craniofacial alterations, as well as melanocytotic tailfins in males (**Figure 1b**). The brain morphology of the turquoise killifish resembles that of a typical teleost (**Figure 1c**) and has been extensively described elsewhere[45]. The turquoise killifish genome contains two paralogs of the human amyloid precursor protein (APP), which encode the amyloid beta (Aβ) sequence, *appa* and *appb* (coding sequences provided in **Supplementary Table 1**). Both paralogs show a highly conserved $A\beta_{1-42}$ sequence from human to killifish from the 11th amino acid onwards ($A\beta_{11-42}$), as well as conserved beta- and gamma-secretase cleavage sites (**Figure 1d**). Alphafold3 indicates similar 3D architecture for killifish (*appa* derived) and human (*APP* derived) $A\beta_{1-42}$ and predicts that despite low conservation at the N' side, killifish $A\beta_{1-42}$ can effectively form multimers (**Extended Data Figure 1a-e**). To investigate whether APP derivatives are detectable in the aged turquoise killifish brain, we performed immunohistochemistry using two Aβ-targeting antibodies. Considering that the available antibodies are not specifically raised against the killifish Aβ peptide, together with the known risks of misinterpretation of non-specific signals in the aged brain[46,47], we first addressed the binding specificity of the antibodies. To that end, we used the 4G8 antibody, targeting the $A\beta_{17-24}$ epitope which is fully conserved between humans and killifish, and can bind full-length APP and various APP derivatives including Aβ. Additionally, we used the pE11 antibody, which targets N-terminally truncated and pyroglutamated Aβ, through recognition of the N-terminal pyroglutamate group and the first six amino acids after truncation ($A\beta_{pE11-16}$) (**Figure 1d**). While 4G8 broadly marks full-length APP and its derivatives, pE11 specifically

123 targets post-translationally modified Aβ ($A\beta_{pE11-40/42}$) in human samples, enabling the tracking of cleaved
124 and toxic Aβ rather than its precursors. We focused on the pE11 antibody over the pE3 antibody, as the
125 pE11 target epitope is conserved between humans and killifish. Even though the 4G8 and pE11 antibodies
126 bind different epitopes of the Aβ peptide, we found a strong co-localization between 4G8 and pE11 signal
127 throughout the anterior rhombencephalon (AR) of aged (6-month-old) killifish (**Figure 1e**). To mitigate
128 the possibility that both antibodies bind the same structure in an epitope-independent manner, we blocked
129 the epitopes by incubating antibodies with synthetic $A\beta_{pE11-42}$ peptide prior to the immunohistochemical
130 staining. While incubation with albumin did not impact the staining pattern of pE11 or 4G8, the signal of
131 both antibodies was almost completely abolished by the pre-incubation with $A\beta_{pE11-42}$ peptide, indicating
132 that both antibodies bind to their targets in the killifish brain through their epitope binding domains
133 (**Extended Data Figure 2a,b**). Noteworthy, while pE11 antibody binding indicates the presence of an
134 APP derivative which is cleaved and pyroglutamated at the 11th amino acid of its Aβ sequence, it does not
135 provide evidence for C' cleavage of APP. Therefore, we hereafter refer to pE11-bound APP derivatives as
136 APP_{pE11}. Taken together, we conclude that the aged turquoise killifish brain contains APP derivatives,
137 including APP_{pE11}.
138

139 **Turquoise killifish develop age-related brain inflammation while expressing key genes involved in**
140 **post-translational APP processing**

141 To investigate the age-dependent mRNA expression levels of *appa* and *appb*, as well as other key genes
142 involved in the biogenesis of APP derivatives, we performed whole brain RNA-sequencing on six young
143 (6-week-old) and six aged (6-month-old) female turquoise killifish (**Supplementary Table 2**).
144 Interestingly, genes downregulated with age indicate a strong decline in cellular proliferation (e.g. *mki67*),
145 consistent with the reported loss of neurogenic potential[24,34,35] (**Extended Data Figure S3a,b**). Genes
146 upregulated with age (e.g., *stat1*, *irf9*, *rsad2*, *cmpk2*) suggest a strong age-related induction of
147 inflammation (**Extended Data Figure 3c**), in agreement with previous findings[24,28,35,36]. To test a
148 potential age-related inflammatory state in the turquoise killifish brain, we adopted markers of brain

149 inflammation in the hypothalamus and optic tectum and tested them via immunohistochemistry by
150 targeting Lymphocyte Cytosolic Protein 1 (LCP1), a pan-leukocyte marker employed to visualize
151 microglia in the zebrafish and killifish brain[24,35,48] (**Extended Data Figure 3d,e**). As LCP1 is an actin-
152 binding protein, the staining pattern visualizes cytoskeletal architecture of brain leukocytes (**Extended**
153 **Data Figure 3f**). We found a strong age-related increase in the surface area covered by LCP1, which
154 validates the age-related inflammatory state suggested by the transcriptomics data (**Extended Data**
155 **Figure 3g**). Next, to adress whether key genes involved in APP derivative biogenesis are actively
156 transcribed in the killifish brain and would support a potential role for APP and it's derivatives during
157 killifish brain aging, we plotted their expression in young and aged brains (**Extended Data Figure 3h**).
158 These genes include amyloid precursor proteins *appa*, *appb*, the APP family members *appl1*, *appl2*, the
159 glutaminyl cyclase *qpctl* which pyroglutamates Aβ, the beta-secretase *bace1* and the family member
160 *bace2* as well as the gamma-secretase subunits *psen1*, *psen2*, *ncstn* and *aph1b*. While all factors showed
161 consistent expression in the turquoise killifish brain, no age-related changes were observed at the mRNA
162 level. In summary, the aging killifish brain becomes subjected to a robust inflammatory state and
163 expresses transcripts encoding key genes involved in the biogenesis of APP derivatives.
164

165 **pE11 signal accumulates across the rostro-caudal axis of the killifish brain**

166 Next, we asked whether *appa* signal detected via 4G8 and pE11 (**Figure 1d,e**) shows any age-related
167 changes. We found that the anterior rhombencephalon (AR) of young, 6-week-old fish, presents 4G8
168 signal covering a similar percentage of the tissue area as in the aged 6-month-old counterparts (**Figure**
169 **2a-c**), possibly reflecting the binding of 4G8 to full-length APP. In contrast, the young AR appears
170 largely devoid of any pE11 signal, while pE11 signal was instead detected in the aged AR (**Figure 2d-f**).
171 These findings suggest that while full-length APP and its derivatives might be present in the brain
172 throughout killifish lifespan, APP_{pE11} accumulates only at a later age. To explore the full spatiotemporal
173 extent of the accumulation of pyroglutamated Aβ, we characterized the pE11 signal in seven different
174 brain regions along the rostro-caudal axis, at four different ages (**Figure 2g**, **Extended Data Figure 4-8**).

175 While the pE11 signal remained nearly undetectable until three months of age, the pE11 covered surface
176 area peaked at six months, which was consistent across all investigated brain regions. At nine months of
177 age, the pE11 covered surface area was decreased compared to the six-month timepoint. To test for
178 possible batch effect explaining signal changes between six and nine months, we repeated this experiment
179 and confirmed the finding in an independent cohort (**Extended Data Figure 9**). The decline in pE11
180 covered surface area between 6- and 9-months of age potentially suggests an increase in clearance, or a
181 reduced production of APP_{pE11}. Alternatively, the reduction of pE11 between 6- and 9-months could be
182 due to the death of $pE11^+$ cells, and/or due to the selective disappearance of animals with high APP_{pE11}
183 levels. Taken together, these results indicate that pyroglutamated APP derivatives accumulate
184 spontaneously across the rostro-caudal axis between 3- and 6-months of age in the brain of the turquoise
185 killifish.
186
187 **APP_{pE11} predominantly localizes intra-neuronally and colocalizes with TUNEL**
188 In the human AD etiology, the APP derivative Aβ is typically known to localize in extracellular beta-
189 sheet aggregates known as Aβ plaques. However, Aβ has also been described to localize
190 intraneuronally[49–54]. We could not identify any large $pE11^+$ or $4G8^+$ extracellular signals indicative of the
191 formation of extracellular amyloid plaques in the aged killifish brain. Instead, we found that 4G8 and
192 pE11 signal mainly localized around nuclei, suggesting a predominantly intracellular localization (**Figure**
193 **1e**, **Extended Data Figure 4-8**). To investigate the potential intraneuronal localization of pE11 in the
194 aged killifish brain, we co-labeled pE11 together with an antibody targeting neuronal nuclei (NeuN).
195 Indeed, pE11 localized directly around $NeuN^+$ nuclei (**Extended Data Figure 10a**), indicating that
196 APP_{pE11} predominantly localizes intra-neuronally. To address whether the intra-neuronal localization of
197 APP_{pE11} is unique to the killifish or whether its localization is evolutionary conserved and also present in
198 aged human brains, we performed pE11 staining on the brains of normal non-pathological (>80 years old)
199 and AD diagnosed individuals (**Extended Data Figure 10b, 11, 12**). Strikingly, we detected
200 intraneuronal pE11 signal in both the cortex and the hippocampus of normal aged human brains, as well

201 as in the brains of Alzheimer's patients. In addition, we detected 4G8 and pE11 signal in extracellular
202 plaques of the Alzheimer's disease brains, which is in line with previous reports[55]. These findings indicate
203 that the occurrence of pyroglutamated APP derivatives is not limited to a specific human pathology, but
204 instead is broadly present the in aged vertebrate brain in an intraneuronal fashion. Pyroglutamated Aβ has
205 been shown to be exceedingly neurotoxic[43]. Therefore, to investigate whether $pE11^+$ cells show signs of
206 DNA double stranded breaks typically indicative of programmed cell death, we adopted TUNEL staining.
207 $TUNEL^+$ cells were nearly undetectable in young killifish brains but were clearly detectable in aged
208 brains (**Extended Data Figure 13, 14a**). Importantly, in aged brains TUNEL signal colocalized with
209 pE11 signal (**Extended Data Figure 14b**), which might suggest that spontaneous accumulation of
210 APP_{pE11} could negatively affect neuronal survival in aged killifish. Indeed, we could detect
211 $TUNEL^+/NeuN^+$ neurons throughout the aging killifish rhombencephalon (**Extended Data Figure 15**), in
212 agreement with previous findings indicating that the aging killifish brain is subjected to substantial
213 neuronal degeneration[29,37–39].
214
215 **APP derivatives aggregate in an age-related manner**
216 The aging killifish brain is characterized by substantial protein aggregation[28–33]. To determine whether
217 this includes Aβ-associated beta-sheet aggregation, we conducted a thioflavin-T assay. This assay detects
218 changes in the fluorescent emission profile of thioflavin-T upon its incorporation into beta-sheet
219 aggregates[56]. Aged brain lysates yielded higher thioflavin-T signal compared to their younger
220 counterparts, indicating an age-dependent increase in beta-sheets protein aggregates (**Extended Data**
221 **Figure 16**). To directly test whether APP derivatives show signs of age-related aggregation, we
222 performed a filter retardation assay, where protein lysates derived from killifish brains of several ages are
223 applied to a filter which retains protein aggregates of a specific size determined by the pore size of the
224 filter [57]. Next, we stained the filter-bound aggregated protein with either the 4G8 or the pE11 antibody.
225 We found that while 4G8 signal was enriched in an age-dependent manner (**Extended Data Figure**
226 **17a,b**), this was not the case for the detected pE11 signal (**Extended Data Figure 17c,d**). Corroborating

227 the potential age-dependent aggregation of $4G8^+/pE11^-$ peptides, we detected an age-dependent increase
228 in intracellular $4G8^+/pE11^-$ puncta in the killifish brain (**Extended Data Figure 18**), which may reflect
229 intracellular aggregation of APP derivatives. Indeed, $4G8^+$ puncta showed a partial overlap with the
230 Aggresome dye, which was previously employed to visualize intracellular protein aggregation in the
231 killifish brain[30] (**Extended Data Figure 19**). The aged human brain display a similar pattern between
232 4G8 and pE11 signals, as the 4G8 signal showed a granulated pattern in contrast to the pE11 staining
233 (**Extended Data Figure 20)**. Taken together, our results indicate that while the aged killifish brain is
234 largely devoid of extracellular plaques, APP derivatives ($4G8^+/pE11^-$) aggregate in an age-dependent and
235 intracellular manner.
236
237 **CRISPR/Cas9 mediated knock-out of *appa* results in reduction of APP derivatives**
238 Given that intraneuronal APP_{pE11} signal as well as $4G8^+$ puncta mark the aged killifish and human brain,
239 we asked whether APP derivatives contribute to brain aging. To test this hypothesis, we generated an
240 amyloid-beta precursor protein a (*appa*) mutant killifish line using CRISPR/Cas9. Using two guide RNAs
241 targeting the second exon of the *appa* gene, we introduced a 16bp deletion leading to a frameshift (**Figure**
242 **3a**). The induced frameshift did not lead to a premature stop-codon but led to a scrambled amino acid
243 coding sequence, which prevented the translation of *appa* derived APP peptide after the second exon,
244 including the amyloid beta coding sequence. In addition to *appa*, we also targeted its homolog, *appb*, for
245 knock-out. While successfully inserting mutations in the *appb* gene, founders could not be raised to
246 adulthood and were therefore excluded from the analysis [58]. The loss of *appb* mutant carriers might
247 indicate a role for *appb* in killifish development, which is in line with the described role for *appb* during
248 early embryonic development in the zebrafish[59]. To investigate whether *appb* compensates the lack of
249 *appa*-derived APP, we performed a Western blot using the 22C11 antibody targeting the full-length APP.
250 22C11 should target both wild-type APPA and APPB, as the epitope targeted by 22C11 is highly
251 conserved in both homologs (16/16 amino acids) and might also detect killifish APLP2 (12/16). APLP1 is
252 less conserved (9/16) and will likely not be detected by the 22C11 antibody. We observed a significant

253 reduction (>50%) of APP levels in the killifish *appa* mutant brain lysates, indicating that the still
254 functional *appb* could not compensate in full for the loss of *appa* derived APP (**Figure 3b,c**). The lack of
255 *appa* in the knock-out fish line did not affect survival rates, nor did the *appa* mutants show specific signs
256 of discomfort (**Figure 3d**). At 6-months of age, the reduced levels of APP led to a reduction in APP
257 derivatives, including APP_{pE11}, indicated by the observed reduction in 4G8 and pE11 immunoreactivity in
258 both the anterior rhombencephalon and hypothalamus superior lobe (**Extended Data Figure 21**, **Figure**
259 **3e-g**). This effect was statistically investigated using a Bayesian model, as it allowed for the bespoke
260 integration of observed slide-to-slide variation in signal intensity. The reduced immunoreactivity of both
261 antibodies in the *appa* mutants further supports their specific binding to *appa* derived peptides. Residual
262 antibody immunoreactivity likely stemmed from *appb* derived peptides. Taken together, the *appa* knock-
263 out killifish line showed reduced levels of APP and its derivatives, including APP_{pE11}.
264
265 **Knock-out of *appa* mitigates brain aging**
266 To investigate the effects of *appa* knock-out on specific aging phenotypes, we took a histological
267 approach and assessed levels of cell death and inflammation. To visualize cell death in the *appa* mutants,
268 we performed TUNEL staining in tissue sections of the anterior rhombencephalon and hypothalamus
269 superior lobe. While $TUNEL^+$ cells were consistently present in brains of wild-type sibling, *appa* mutant
270 brains contained a lower $TUNEL^+$ covered surface area in both investigated regions at as early as 6-
271 months of age (**Figure 3h-j**). To further validate the potential mitigation of age-related inflammation, we
272 performed an immunohistochemical staining using an antibody targeting Lymphocyte Cytosolic Protein 1
273 (LCP1) as previously described (**Extended Data Figure 3d-f**). The 6-months-old *appa* mutant brain
274 displayed a significant reduction of LCP1 covered surface area in the hypothalamus superior lobe, but not
275 in the anterior rhombencephalon (**Figure 3k-m**).
276
277 To investigate the effects of the knock-out of *appa* in an unbiased manner, we performed liquid
278 chromatography mass spectrometry (LC-MS) on whole brain lysates (**Supplementary Table 3**). We used

279 three males and three females from both *appa* mutants, as well their wild-type siblings, for each of the
280 two age groups (6- and 7.5-month-old). We chose the 7.5 months time-point as it corresponds to the
281 median lifespan of fish from the ZMZ1001 strain (**Figure 1a**), when behavioral changes become apparent
282 and therefore corresponds to a critical timepoint to assess brain aging phenotypes related to cognition[39,41].
283 At both timepoints, *appa* derived peptides were undetectable in the *appa* mutants, while *appb* derived
284 peptides (APPB) showed no significant changes (**Figure 3n, Extended Data Figure 22a**). At 6-months
285 of age, the *appa* mutants displayed an upregulation of proteins involved in mitochondria (e.g., DHRS12,
286 SLC25A3, NDUFV1), translation (e.g., RPS7, RPL27, RPS13), and DNAJ-chaperones (e.g.,
287 DNAJC5AA, DNAJA1L, DNAJB3, DNAJA3A), as well as a downregulation of amyloidosis associated
288 factors Apolipoprotein A1 (APOA1) and beta-synuclein (SNCB) (**Figure 22a,b**). Compared to same-aged
289 wild-type siblings, 7.5-month-old *appa* mutants showed an upregulation of keratins (e.g., KRT4, KRT5,
290 KRT18) and a downregulation of proteins involved in the lysosome and proteasome, as well as proteins
291 involved in inflammation related ontologies, such as the defense response (e.g., C4B, TGFB1) and the
292 JAK-STAT cascade (e.g., STAT1A). In addition, we observed downregulation of proteins involved in
293 necroptosis (e.g., MLKL, XIAP) which is suggestive of a reduction in programmed cell death (**Figure**
294 **3n,o**)[59] . Taken together, the LC-MS and histological findings indicate that the knock-out of *appa*
295 mitigates spontaneous cell death and inflammation in the aging turquoise killifish brain.
296
297 To determine whether the changes in protein abundances upon *appa* knock-out represent a broader
298 mitigation of brain aging, we investigated whether we could detect a proteome-wide shift towards a
299 younger state in the *appa* mutants compared to their wild-type siblings. To this end, protein group
300 abundances were compared between young (6-week-old) and aged (6-month-old) brains, as well as
301 between *appa* mutant and wild-type sibling brains at two different ages (6 and 7.5 months). Subsequently,
302 the log2 fold-change (log2FC) values from both the young-versus-old and *appa* mutant-versus-wild-type
303 comparisons were plotted against one another. In 6-month-old *appa* mutants, the differentially abundant
304 proteins did not correlate with age-related changes in protein level (**Figure 22c**). However, in 7.5-month-

305 old *appa* mutants, we observed a highly significant negative correlation (slope = -0.265, p = 2.31e-13)
306 indicating that proteins upregulated with age were downregulated in the mutants, and *vice versa* (**Figure**
307 **3P**). Proteins upregulated with age but downregulated in the *appa* mutants included proteins implicated in
308 neurodegenerative diseases (e.g., APOEB, PFN1, LGALS9) and inflammation (e.g., IFI44L, C4B,
309 CMPK2), while proteins downregulated with age and upregulated in the *appa* mutants included
310 extracellular matrix components (e.g., COL1A2, KRT5) as well as proteins involved in neuronal function
311 (e.g., GRM8, PCDH2AC, PPFIA2). These findings indicate that *appa* knock-out mitigated brain aging in
312 a proteome-wide manner between 6- and 7.5 months of age, extending beyond the reduction of
313 inflammation and cell death.
314
315 **Knock-out of *appa* mitigates age-related learning decline**
316 Turquoise killifish display a spontaneously occurring decline in learning capacity with age, a *bona fide*
317 measure of age-related cognitive decline[39,41]. To investigate whether *appa* contributes to non-pathological
318 age-dependent learning deficiency, we developed an active avoidance test based on previous
319 literature[39,60,61]. Each fish (28 *appa* mutants and 30 wild-type siblings) was individually tested in an arena
320 consisting of two circular compartments, connected through a narrow opening (**Figure 4a**). After a 15-
321 minute acclimatization period, fish were subjected to 40 consecutive cycles, where a conditionate
322 stimulus (light), was coupled with a non-conditioned stimulus (air bubbles). Each one-minute cycle
323 corresponded to 30 seconds of light exposure, with the latter 15 seconds combined with exposure to air
324 bubbles, followed by a rest phase of 30 seconds. Untrained fish showed a preference to remain in the
325 light, with 84% of the fish staying within the light during the first cycle of the experiment (**Figure 4b**).
326 Due to the pairing of the light with an adverse non-conditioned stimulus (air bubbles) across the 40
327 cycles, the fish learn to avoid air bubbles once cued with light. Indeed, even 7.5-month-old wild-type fish
328 (n = 30) become increasingly proficient at actively avoiding the light with 16% (first cycle) to 46% (last
329 cycle) of the fish escaping the bubbles (**Figure 4b**, **Extended Data Figure 23**, **Supplementary Table**
330 **4**). However, the 7.5-month-old *appa* mutants (n = 28) outperform their age-matched wild-type siblings

331 and show an increased rate of successful escapes after the 6th cycle onwards, while reaching an average
332 escape rate of 55% during the last cycle (**Figure 4b**, **Extended Data Figure 23**). Comparing the total
333 amount of successes, as well as their top scores, defined as the maximum number of successes in a 10-
334 cycle window, show higher (yet non statistically significant) learning performance in the *appa* -/- mutants
335 ($p = 0.073$ and $p = 0.265$, respectively) (**Figure 4c,d**). Significant improvements in the *appa* -/- mutants
336 were observed when comparing the speed at which their top scores were reached (**Figure 4e**) and when
337 considering both top scores and the speed (i.e. the number of the learning cycle) at which the top score
338 was reached simultaneously (**Figure 4f**). To gain insight into the biological significance of the learning
339 improvements observed in the *appa* -/- mutants at 7.5-months of age, we performed the active avoidance
340 test on an independent cohort of young killifish (6-week-old, n = 16) (**Extended Data Figure 24**). While
341 young fish show a higher escape rate in the first 5 cycles of the experiment compared to all other non-
342 young counterparts, the 7.5-month-old mutants performed not only better than age-matched controls, but
343 similar to young fish for the remaining cycles. These results suggest that knock-out of *appa* can almost
344 completely rescue the age-related learning deficit observed in turquoise killifish.
345
346 Newly learned behaviors (e.g. the negative association with red light) are encoded within a neuronal
347 network which, upon activation, expresses the immediate response factor c-Fos[62,63]. To address whether
348 the active avoidance test we employed led to the activation of such network, and whether the *appa*
349 mutants show increased network activity compared to their wild-type siblings, we used Hybridization
350 Chain Reaction (HCR) *in situ* mRNA detection. We used HCR to visualize *fos* transcripts in brains
351 isolated immediately after the 40th cycle of the active avoidance task (**Figure 4g-j**). We specifically
352 quantified the percentage surface area covered by *fos* transcripts in the medial zone of the telencephalon
353 (**Figure 4k**), considering that this region has been previous implicated in learning performance of other
354 fish species[64]. We found that the *appa* mutants that underwent the active avoidance test showed higher
355 *fos* levels in the medial zone when compared to untested fish, as well as their wild-type siblings that did
356 undergo the active avoidance test (**Figure 4l**). From these results, we conclude that the knock-out of *appa*

357 rescued an age-induced learning deficit, which is associated with enhanced neuronal activity in the
358 telencephalon.
359
360
361

362 **Discussion**

363

364 In this study, we asked whether the detrimental effect of APP derivatives on the brain is limited to
365 neurodegenerative diseases, or whether APP derivatives also impact normal, non-pathological brain
366 aging. Although APP derivatives (e.g. $A\beta_{1-42}$) has been shown to accumulate during normal aging[65],
367 convincing experimental proof of its causal effect remained absent. An important clue suggesting a
368 potential causal effect of APP derivatives in the normal aging brain was provided by a previous study
369 describing the cognitive fitness of aged human carriers of the Islandic APP variant (A673T). The A673T
370 APP mutation leads to a reduction in β-Secretase 1 (BACE1)-mediated Aβ production[66], which not only
371 correlated with a reduced risk to develop Alzheimer's disease (AD), but also with increased cognitive
372 fitness in normal aging individuals[67]. In addition, a negative correlation was found between amyloid
373 burden and cognitive performance in non-pathological centenarians[68]. Here, we provide the first
374 experimental evidence showing that lowering APP levels in spontaneously aging vertebrates can reduce
375 brain aging phenotypes and mitigate age-related cognitive decline.

376

377 To investigate the effect of APP during normal brain aging, we have employed the turquoise killifish.
378 These annual teleosts evolved a compressed lifespan due to the genome-wide accumulation of risk alleles,
379 largely driven by past population bottlenecks[69]. Therefore, the aging phenotypes observed in the turquoise
380 killifish brain are most likely a consequence of their exceptionally high mutation load and have a
381 polygenic basis. Due to their short lifespan, turquoise killifish represent an ideal model for functional
382 studies investigating vertebrate aging. In this study, we recapitulate previously reported brain aging
383 phenotypes of the turquoise killifish, including the aggregation of protein, inflammation, and cellular
384 degeneration. Furthermore, we describe an additional brain aging phenotype, the intraneuronal
385 accumulation of APP_{pE11}. Notably, we found that intraneuronal APP_{pE11} not only characterizes the aging
386 brain of the killifish but is also present in aged, non-diseased human brains. Intraneuronal APP_{pE11} had
387 previously been associated with Alzheimer's disease[70] but, to the best of our knowledge, remained

388 unexplored in the context of normal brain aging. While $A\beta_{pE3}$ is expressed and studied in AD mouse
389 models (e.g. 5xFAD)[71], no animal data were available to date for the endogenous expression of APP_{pE11}.
390 Several mechanisms could explain intraneuronal APP_{pE11} accumulation during aging, including an age-
391 dependent increase in APP endocytosis[72] further processed in the *trans*-Golgi network[73,74,75], or a decline
392 in APP_{pE11} clearance efficiency.
393
394 To test the impact of APP during normal aging, we knocked out one the amyloid-beta precursor protein
395 coding genes, *appa*. Both the histological and LC-MS results indicated that *appa* knock-out mitigated
396 cellular death and inflammation in aged killifish brains. Furthermore, proteome-wide analysis indicated
397 that the beneficial effects of *appa* knock-out are not restricted to inflammation and cell death but
398 encompass a much broader, proteome-wide mitigation of brain aging. The beneficial effects of *appa*
399 knock-out on brain aging in the turquoise killifish is in stark contrast with the negative effects observed in
400 APP knock-out mice, which are viable but have altered neurogenesis and smaller brains[78]. In addition,
401 aged APP knock-out mice display increased reactive gliosis in the neocortex and hippocampus and show
402 reduced locomotor activity[79], as well as reduced memory retention[80]. It has been suggested that both
403 excessive amounts of Aβ, as well as complete depletion of Aβ, has negative effects on brain
404 functionality[81]. As teleosts, turquoise killifish have been subjected to a whole genome duplication[82] and
405 hence, contain two APP paralogues. Therefore, while knockout of APP in mice resulted in a complete
406 depletion of Aβ, knock-out of *appa* in killifish left the fish with *appb*, which might have yielded a
407 concentration of Aβ high enough to allow typical brain development and function, but low enough to
408 evade Aβ-mediated exacerbation of brain aging phenotypes.
409
410 While decades of research have focused on elucidating the effects of APP and its derivatives during
411 Alzheimer's disease, the effects of APP during normal aging remained largely unexplored. Here, we show
412 that APP exacerbates brain aging in a short-lived teleost. These findings indicate that the detrimental
413 effects of APP and its derivatives are not limited to a specific human pathology, but could instead broadly

414 impact vertebrate brain aging. APP-targeting strategies, originally intended to mitigate neurodegenerative
415 diseases, may therefore have broader potential as an anti-aging approach to preserve cognitive health
416 throughout life.
417

418 **Methods**

419

420 *Fish husbandry and maintenance*

421 The turquoise killifish (ZMZ1001 strain) were housed in individual 2.8L tanks equipped with baffles, fry
422 mesh and lids glass capillaries (Aquaneering, USA) connected to a system with circulating water. Fish
423 received 12 h of light and 12 h of darkness per day. Water temperature was set to 28°C. Fish were fed
424 with brine shrimp nauplii (*Artemia salina*) and blood worm larvae (*Chironomus spp.*) twice a day during
425 the week and once a day during the weekend. Adult fish (6 weeks post hatching) were used for breeding
426 purposes. One male and up to three females were housed in 9.5L breeding tanks equipped with baffles,
427 fry mesh and lids glass capillaries (Aquaneering, USA). Fertilised eggs were regularly collected using
428 sand boxes and then stored in a petridish with coconut fiber at 24°C. Three weeks prior to hatching,
429 embryos were placed at 28°C. Furthermore, the husbandry and maintenance of the killifish used in this
430 study were performed as part of the standard operating procedure the Leibniz institute on Aging, which
431 was described in detail in a previous publication[83]. The experiments were carried out under permission of
432 the following animal experimental licenses: FLI-21-016 (young behavioral tests), FLI-23-029 (appa KO
433 versus wild-type behavioral tests), Par.11 J-003798 (Maintenance and Housing), FLI-22-203
434 (Genotyping), O-DV-23-27 (Organ harvest license).

435

436 *Protein alignment and Alphafold protein structure predictions*

437 To determine how similar protein sequences of APPA and APPB from turquoise killifish are to protein
438 sequences from humans (*H. sapiens*), mice (*M. musculus*) and zebrafish (*Danio rerio*), full-length peptide
439 sequences were aligned using UniPro UGENE (RRID:SCR_005579). Multiple protein sequences were
440 aligned with the MUSCLE default mode. The sequences of all protein variants from online database
441 Ensembl (https://www.ensembl.org/index.html). Structure predictions of $A\beta_{1-42}$ were performed using the
442 AlphaFold3 web server with default options[84]. For graphical representations the program ChimeraX[85] was
443 employed.

444

445 *Brain processing for cryo-sectioning*

446 Killifish were euthanized using rapid-chilling method. The whole head was first fixed in 4%
447 paraformaldehyde overnight at room temperature. The next day brain was isolated, washed in 4% sucrose
448 and incubated in 30% sucrose overnight at 4°C. On the last day, brain was transferred to an appropriate
449 Tissue-Tek cryomold, immersed in the Tissue-Tek O.C.T. Compound and transferred to the dry ice to
450 quickly freeze the tissue. Brains were stored at -80°C until the sectioning step. The tissue blocks were
451 sectioned to 10 µm thin sections using cryostat machine, while following standard protocol for cryo-
452 sectioning.

453

454 *Immunohistochemistry, imaging and quantification*

455 Thawed slides were first washed in PEMTx solution (80 mM 98.5+% PIPES (1,4-Piperazin-bis-
456 (ethansulfonacid), 5 mM EGTA, 1 mM $MgCl_2$, 0.2% Triton X-100 in milliQ water, pH 7,5) for 10 min, in
457 NH_4Cl-PEMTx (50 mM of NH_4Cl in PEMTx) for another 10 min, and then two more times in PEMTx.
458 The slides were transferred and incubated in Sodium Citrate Solution (10 mM 99% Trisodium Citrate
459 Dihydrate in RO H_2O, pH 6) for 15 min at 85°C in the waterbath. Once cooled down to the room
460 temperature, slides were washed two times for 10 min in PEMTx. The tissue was incubated in the
461 blocking solution (10% Fetal Bovine Serum, 1% DMSO in PEMTx) for 1 hour at room temperature in a
462 humidified chamber. Slides were later incubated with primary antibodies diluted in a blocking buffer at
463 4°C overnight in a humidified chamber. The following day, the slides were washed in PEMTx solution
464 five times for 20 min (on a shaker). The slides were incubated in the secondary antibody (1:500) and
465 DAPI (1:1000) diluted in a blocking buffer for 1 h at room temperature in a humidified chamber and in
466 the dark. The primary antibody Rabbit Anti-Abeta-pE11 was combined with the secondary antibody
467 Alexa Fluor® 647 Donkey anti-rabbit IgG (min. x-reactivity) antibody (BioLegend, USA, Cat# 406414,
468 RRID: AB_2563202). The Rabbit Anti-GFAP antibody was combined with the secondary antibody Alexa
469 Fluor 555 (Thermo Fisher Scientific, USA, Cat# A-21428, RRID: AB_2535849). The slides were washed

470 in PEMTx solution five times for 10 min, then two times for 7 min in PEM solution (80 mM 98.5+%
471 PIPES (1,4-Piperazin-bis-(ethansulfonacid), 5 mM EGTA, 1 mM $MgCl_2$ in miliQ H_2O) on the shaker and
472 in the dark. Slides were mounted in the ProLong Gold antifade reagent and stored at 4°C in the dark. The
473 slides were imaged using Zeiss Axio Scan.Z1 microscope with a Plan-Apochromat 20x/0.8 M27
474 objective, Axiocam 506m imaging device and 1x Camera Adapter. Imaging results were processed using
475 ZEN 3.5 (Blue Edition) ZEN Digital Imaging for Light Microscopy (RRID:SCR_013672) to select
476 images and Fiji (ImageJ2, RRID:SCR_002285) and Imaris (V10.2, 2024 June 26) to quantify positive
477 signal. Positive signal was defined as the percentage of the surface area within a given brain region that
478 was covered by staining. For each brain region and individual, three sections were analyzed, and mean
479 values were calculated for presentation in the figures.
480
481 *Signal intensity measurements and Bayesian statistical analysis*
482 Brains from *appa* wild-type and mutant fish were isolated and embedded in pairs. Sectioning at
483 10 µm thickness generated slides containing both wild-type and mutant tissue.
484 Immunohistochemistry was performed using the 4G8 and pE11 antibodies. Signal intensity was
485 quantified as the mean pixel intensity across the tissue-covered area within defined brain regions
486 (Figure 3g, Figure S21c). We quantified the signal intensity of 4G8 and pE11 in the *appa*
487 mutants, instead of the signal covered surface area, as we observed that while the covered
488 surface area remained relatively stable, the signal intensity appeared visibly reduced. For each
489 brain region and individual, three stained sections were analyzed.
490 Imaging was carried out using a Zeiss Axio Scan.Z1 microscope equipped with a Plan-
491 Apochromat 20×/0.8 M27 objective, an Axiocam 506m camera, and a 1× camera adapter. Image
492 acquisition and signal quantification were performed with ZEN 3.12 software.

493 Because *appa* wild-type and mutant brains were embedded and sectioned together, we were able
494 to observe slide-to-slide variability in average signal intensity, despite consistent staining and
495 imaging protocols. To account for this, we applied a Bayesian model to estimate the genotype
496 effect (wild-type – knockout) on immunoreactivity. This approach incorporated slide-to-slide
497 variation as a covariate and yielded posterior distributions from which confidence intervals were
498 derived.
499
500 *Immunohistochemistry on human brain samples*
501 Human brain tissue samples of AD patients and aged-matched controls were obtained from the London
502 Neurogenerative Diseases Brain Bank, King's College London. For each individual, we used consecutive
503 tissue sections of 10 um thickness in order to visualize the precise localization of the staining for 4G8 and
504 pE11 in comparable areas.
505 Tissue sections deriving from 2 AD patients (BBN-ID: BBN_9888, 80, M, and BBN_002.34142, 77, M)
506 and 2 control individuals (BBN-ID: BBN002.36178, 86, M, and BBN_23398, 83, M) were
507 deparaffinized in two changes of xylene of 5 minutes each, followed by rehydration through a graded
508 series of ethanol (100%, 96%, 70%, 50%) for 5 minutes at each concentration and finally rinsed in
509 distilled water for 5 minutes. Acid antigen retrieval was performed using citrate buffer (10 mM, pH 6.0,
510 Tween 20, 0.05%) in a microwave oven. Tissue sections were submerged in the buffer and heated for 3
511 minutes at 95°C. After cooling to room temperature, the sections were washed in phosphate-buffered
512 saline (PBS, pH 7.4) three times for 5 minutes.
513 Endogenous peroxidase activity was quenched by incubating the sections in 3% hydrogen peroxide
514 (H_2O_2) in water for 10 minutes at room temperature, followed by two washes in PBS for 5 minutes each.
515 To reduce nonspecific binding, sections were incubated with normal serum (from the species of the
516 secondary antibody host) provided by the kit (ImmPRESS® HRP Goat Anti-Rabbit IgG Polymer Kit and

517 ImmPRESS® HRP Horse Anti-Mouse IgG Polymer Kit, MP-7451 and MP-7402, Vector Laboratories)
518 for 2 hours at room temperature.
519 Tissue sections were then incubated with the primary antibody (pE11, Synaptic Systems, 1:200 dilution
520 or 4G8, Biolegend, 1:500 dilution) diluted in PBS with 1% bovine serum albumin (BSA) and 0.1% Triton
521 X-100. Sections were incubated overnight at 4°C in a humidified chamber.
522 The day after, sections were rinsed in PBS three times for 5 minutes each. Sections were then incubated
523 with the appropriate HRP conjugated secondary antibody belonging to the kit for 1 hour at room
524 temperature. After washing with PBS (3 × 5 minutes), immunoreactivity was visualized using 3,3'-
525 diaminobenzidine (DAB) chromogen solution prepared according to the manufacturer's instructions
526 (DAB Peroxidase Substrate, SK-4100, Vector laboratories). Sections were incubated with DAB for 4-5
527 minutes, monitoring the color development under a light microscope. The colorimetric reaction was
528 stopped by rinsing the slides in distilled water.
529 For counterstaining, sections were immersed in hematoxylin for 3 minutes, rinsed in tap water, and
530 dehydrated through graded alcohols (50%, 70%, 96%, and 100%) followed by xylene. Finally, sections
531 were coverslipped with a permanent mounting medium (Permount mounting medium, SP15-100, Fisher
532 Chemical).
533 Additionally, we performed in parallel the same procedure on a sample from a control individual as
534 negative control, i.e. we treated the sections as described above, omitting only the addition of any primary
535 antibody to the solution prior to the overnight incubation.
536 Immunostained sections were then imaged using a light microscope (Nikon Eclipse600) equipped with a
537 DS-Fi3 color camera (Nikon, Tokyo, Japan) and a double LED light O-ring.
538
539 *PROTEOSTAT aggresome staining*
540 To detect intracellular protein aggregation, we used the PROTEOSTAT® Aggresome detection kit (ENZ-
541 51035, Enzo Life Sciences). In short, following the immunohistochemical detection of 4G8, slides were
542 incubated for 30 minutes in a dark humidified box with Aggresome staining solution (1:500). Next, slides

543 were washed three times in PBS, followed by mounting in prolong gold. Imaging was done using Ex/Em
544 wavelengths of 550 – 565-600nm, respectively.
545
546 *Used antibodies:*

Antibody	**Used for**	**Dilution**	**Ordering details**
Rabbit polyclonal purified Anti-Abeta-pE11	IHC	1:200	Synaptic Systems, AB_2619913
Mouse anti APP A4 clone 22C11	WB	1:5000	Millipore, MAB348
anti-mouse IgG HRP conjugate	WB	1:10000	Promega, W402B
Mouse anti-a-tubulin	WB	1:100000	Sigma, T6199
Anti-Acetylated Tubulin, Mouse Monoclonal (Clone 6- 11B- 1)	IHC	1:100	Sigma-Aldrich, T7451
Anti-β-Amyloid, 17-24 Antibody (4G8), mouse monoclonal	IHC	1:100	Biolegend, SIG-39200
Anti-LCP1, rabbit polyclonal	IHC	1:100	GeneTex, GTX124420
Anti-NeuN, mouse monoclonal (clone A60)	IHC	1:150	Sigma-Aldrich, MAB377
Anti-rabbit Alexa555 (IgG, H+L)	IHC	1:500	Invitrogen, A21428
Anti-rabbit Alexa647 (IgG, H+L)	IHC	1:500	Invitrogen, A27040
Anti-mouse Alexa555 (IgG, H+L)	IHC	1:500	Invitrogen, AB_2535844
Anti-mouse Alexa647 (IgG, H+L)	IHC	1:500	Invitrogen, A21235
Anti-rabbit-HRP	FRA	1:5000	Dianova
Anti-mouse-HRP	FRA	1:2000	Sigma-Aldrich

547
548 *RNA sequencing*
549 Brain dissection was followed by RNA isolation using the TRIzol reagent (Life Technologies, Carlsbad,
550 CA, USA) according to the manufacturer's instructions. RNA integrity and concentration were measured
551 using Agilent 4200 TapeStation System in combination with RNA ScreenTape (Agilent Technologies,
552 Santa Clara, CA, US) ensuring high quality RNA (RNA Integrity Numbers > 8) for library preparation.
553 Libraries for Illumina next-generation sequencing technology[86] were prepared from 200 ng of total RNA
554 using NEBNext Ultra II Directional RNA Library Preparation Kit in combination with NEBNext Poly(A)

555 mRNA Magnetic Isolation Module and NEBNext Multiplex Oligos for Illumina (Unique Dual Index UMI
556 Adaptors RNA) following the manufacturer's instructions (New England Biolabs, Ipswich, MA, US).
557 Library quantification and quality assessment were performed using Agilent 4200 TapeStation System with
558 D5000 ScreenTape. Libraries were then pooled and sequenced on NovaSeq 6000 platform (Illumina, San
559 Diego, CA, US) using the SP 100 cycle v1.5 kit with a 51-cycle paired-end read configuration. A minimum
560 sequencing depth of 33.2 million reads per sample was achieved. Sequencing data were converted to
561 FASTQ format using bcl2fastq (v2.20.0.422).
562
563 *RNA sequencing data analysis*
564 Raw sequencing data (FASTQ files) were evaluated for quality using FastQC (v0.11.9). Adapter sequences,
565 poly-A sequence and low-quality bases were removed using cutadapt (v4.2). High-quality reads were
566 aligned to the reference genome (*Nothobranchius furzeri*, MPIA_NFZ_2.0) using STAR (2.7.6a) and PCR
567 duplicates were removed based on unique molecular identifiers by umi-tools (1.1.1, parameter: --chimeric-
568 pairs discard --unpaired-reads discard –paired). Gene-level quantification was performed using
569 featureCounts (v2.0.3, parameter: -s 2 -p -B --countReadPairs) based on annotated gene features (obtained
570 through personal communication with David Willemsen, corresponding to[87]. Differentially expressed genes
571 were obtained using the R package EdgeR[88] and gene ontologies were obtained using the online tool
572 DAVID[89].
573
574 *TUNEL staining*
575 To visualize apoptotic cells in the killifish brain, cryosections (fixed in 4% PFA, sectioned 10um thick)
576 were stained using the In Situ Cell Death Detection Kit, TMR rot (12156792910) from Roche. In short,
577 cryosections were air dried for 15 seconds, and washed in PBS + 0,2% Triton-X100 for 3 times 10
578 minutes. Three washes in PBS, of each 5 minutes, were followed by placing the slides in a humidified
579 box, and the brain sections of interest were encircled by a hydrophobic pen. Next, TUNEL staining
580 solution was added on top of the sections which were placed, inside of the humidified box, in a 37°C

581 incubator for 60 minutes. Afterwards, the slides were washed 3 times for 5 minutes in PBS and incubated
582 with PBS+ DAPI (1:000 dilution) for 20 minutes in the humidified box. Last, the slides were washed 3
583 times for 5 minutes with PBS and mounted using Prolong Gold. Imaging and quantification were
584 performed as described for immunohistochemistry, utilizing TUNELs excitation spectrum at 540nm and a
585 emission spectrum between 570-620nm.
586
587 *Western blot analysis*
588 Liquid frozen brains of killifish appa -/- and age matched controls of 6-months of age were lysed in
589 300µls 4xLämmli sample buffer (4 ml 20% SDS, 4 ml glycerol, 1ml ß-mercaptoethanol, 1 pinch
590 bromophenol blue, 1,25 ml 1M Tris pH 7,6) using a tissue homogenizer. After boiling for 10 min at 95°C
591 while shaking at 600 rpm, the samples were centrifuged 1 min at 11000 rpm. 20µls of the total lysate
592 were loaded on Schägger gels. After 60 mins transfer to nitrocellulose blotting membrane (0,1 µm,
593 Amersham™ Protran, product 10600005) at 400 mA, the membrane was boiled for 5 mins in 1 x PBS,
594 then incubated in 1 x PBS for 30 mins at room temperature before blocking with 0,2% Tropix I-Block
595 (Applied Biosystems) for 1 hr at room temperature on a rotating platform. The incubation in primary
596 antibody 22C11 (Mouse anti APP A4 clone 22C11, Millipore MAB348, 1:5000 in I-Block) was done
597 overnight at 4°C. After removal of the primary antibody, the membrane was washed 4 x 15 mins in I-
598 Block, followed by 1 hr incubation in a 1:10000 dilution of the secondary antibody (anti-mouse IgG HRP
599 conjugate, W402B, Promega) at room temperature. The membrane was washed 4 times 15 mins and 3
600 times 10 mins with 1 x PBS before detection of bound antibodies with ECL plus (Pierce ECL Plus
601 Western Blotting substrate, Thermo Scientific). After images were acquired using the LAS-4000 image
602 reader (Fujifilm Life Science), the membrane was washed 4 x 15min in PBST, blocked in 3%milk for 1hr
603 at room temperature and then incubated with the primary anti-a-tubulin antibody T6199 (Sigma) 1:100
604 000 in I-Block overnight at 4°C. After removal of the anti-a-tubulin antibody antibody, the membrane
605 was washed 4 x 15 min in I-Block, followed by 1 hr incubation in a 1:10000 dilution of the secondary
606 antibody (anti-mouse IgG HRP conjugate, W402B, Promega) at room temperature. The membrane was

607 washed 4 x 15 min and 3 x 10 min with 1 x PBS before detection of bound antibodies with ECL plus
608 (Pierce ECL Plus Western Blotting substrate, Thermo Scientific). Images of 22C11 and a-tubulin were
609 quantified with the software ImageJ. For each group biological triplicates were quantified.
610
611 *Thioflavin-T assay*
612 Whole brain protein lysates were produced using the same protocol as described to LC-MS. Black and
613 transparent bottom 96-well plate (Greiner 96 F-bottom, Thermo Fisher #165305) were used, as well as the
614 CLARIOstar Plus (BMG Labtech) plate reader. Thioflavin-T powder was bought from Sigma-Aldrich
615 (T3516). To produce the Thioflavin-T (ThT) working solution, 80mg of ThT-powder was added to 25mL
616 of dPBS (Gibco, [-] Cacl [-] MgCl) to make a 10mM stock. The solution was vortexed and incubated for
617 1 hour at room temperature. After the almost complete dissolvement of the ThT, 10mL of the ThT
618 solution was filtered through a 0.2µm filter using a syringe. Next, 200µl of the filtered ThT solution was
619 added to 1700µl of dPBS, to make the working solution of 50µM, and kept in the dark until further use.
620 Next, protein lysates (49µl of 1.325µg/µl) was added to the 96-well plate (F-bottom). Using a
621 multichannel pipet, 1µl of the ThT working solution (50µM) was added to the wells, and the plate was
622 entered in the plate reader directly. The following imaging settings were used: Microplate: Greiner 96 F-
623 bottom; Presets: CFP; Exitation: 430-20nm; Dichroic: auto 455nm; Emission: 480-20nm; Well scan:
624 none; Optic: Bottom optic; Settling time: 0.2; Flying mode: off; No. of kinetic windows: 1; No. of cycles:
625 10; No. of flashes: 50; Cycle time: 60; Shake: Before first cycle; double orbital, 100rpm, 10sec. Values
626 were recorded after 3 minutes and 30 seconds. Biological replicates were used in duplo, and averaged
627 values were plotted.
628
629 *Filter retardation assay*
630 Brain tissues were transferred to 2 mL Precellys tubes containing a mix of 1.4 mm and 2.8 mm ceramic
631 (zirconium oxide) beads, in 200 µL of BPS-PIS buffer. Two cycles of mechanical homogenization were
632 carried out at 6000 rpm for 30 seconds each, with a 30-second break on ice between each cycle, using the

633 Precellys 24 lysis and homogenizer (Bertin, France). Subsequently, the tubes were centrifuged at 3000
634 rpm for 5 min at 4°C. The resulting supernatant was carefully transferred to a new 1.5 mL low-binding
635 tube. An equal volume of 2X lysis buffer was added to the homogenate and sonicated (Bioruptor Plus,
636 Diagenode, Belgium) for 20 cycles (60 sec ON/30 sec OFF) at 4°C. The protein concentration in the
637 lysate was quantified using the Pierce™ BCA Protein Assay Kit (Thermo Fisher Scientific, Cat. no.
638 23227). For the filter retardation analysis, we adapted a previously published protocol[57]. In brief, 100 µg
639 of protein was loaded in duplicate onto a 0.2 µm cellulose acetate membrane (Cytiva, Cat. no. 10404180)
640 that had been pre-equilibrated in 1X TBS. The membrane was washed twice with a wash buffer (150 mM
641 NaCl and 10 mM Tris, pH 8.0), then blocked with 5% milk. This was followed by incubation with
642 primary antibodies: Rabbit-anti-pE11 (1:500, Synaptic Systems) or Mouse-anti-4G8 (1:1000,
643 BioLegend), overnight. Subsequent incubation with secondary antibodies was performed using anti-
644 rabbit-HRP (1:5000, Dianova) and anti-mouse-HRP (1:2000, Sigma-Aldrich) for 4 h. The images were
645 captured in Amersham imager 600, and quantification was performed using Fiji ImageJ software. Buffers:
646 BPS-PIS: 250 µL PBS; 5 µL Protease inhibitor cocktail; 25 µL PhosSTOP. Lysis Buffer (2X): 225 µL
647 PBS; 25 µL SDS (10%); 12.5 µL HEPES (2M). Tris-buffered saline (TBS) 10X, pH 8: 200 mM Tris
648 base; 1.5 M NaCl. Tris-buffered saline with Tween (TBS-T): 1X TBS; 0.1% Tween 20.
649
650 *CRISPR/Cas9 transgenesis*
651 CRISPR/Cas9 tool was used to edit the genome of the turquoise killifish. Guide RNA templates were
652 designed using an online program CHOPCHOP (https://chopchop.cbu.uib.no/). Exon 2 of *appa* was
653 targeted using two different gRNAs, and Exon 3 of *appb* was targeted using three different gRNAs.
654 Templates of ssDNA target-specific oligonucleotides were used for sgRNA synthesis. Used guide RNA's
655 (regions in bold indicate the complement sequence of the target):

***appa* sgRNA1**	TAATACGACTCACTATAGG**TCAACGTTCAGAGCGGCAAG**GTTTTAGAGCTAGAAATA GCA
***appa* sgRNA2**	TAATACGACTCACTATAGG**CAAGTGGGAGTCCGACCCCT**GTTTTAGAGCTAGAAATAGCA
***appb* sgRNA 1**	TAATACGACTCACTATAGG**AAACCCACCGAGTCATCCAAAG**GTTTTAGAGCTAGAAATAGCA

***appb* sgRNA 2**	TAATACGACTCACTATAGG**ACAGATCACGAATGTCGTAG**GTTTTAGAGCTAGAAATAGCA
***appb* sgRNA 3**	TAATACGACTCACTATAGG**CATTCGTGATCTGTAGCTCT**GTTTTAGAGCTAGAAATAGCA

656

657 The template ssDNA target-specific oligonucleotide to synthesise gRNA was designed by adding an
658 overlapping nucleotide sequence to the N-terminus and T7 promoter sequence to the C- terminus. The
659 PAM sequence (NGG) was removed from the sequence. Templates were synthesised and delivered by the
660 Integrated DNA Technologies (https://eu.idtdna.com/pages/products/custom-dna-rna/dna-oligos). The
661 sgRNAs were synthetised using the EnGen® sgRNA Synthesis Kit (New England BioLabs, USA,
662 #E3322V), according to their standardized protocol. The synthesised sgRNAs was cleaned up with the
663 Monarch® RNA Cleanup Kit (50µg, New England BioLabs, USA, #T2040L), following the instructions.
664 For CRISPR/Cas9 injections, concentration of sgRNA solution was adjusted to 300 ng/µL. The
665 CRISPR/Cas9 and gRNA reaction mix was prepared with EnGen® Spy Cas9 NLS (20 µM, New England
666 Biolags, USA), by mixing 1 µL of Cas9 NLS, 1 µL of each purified sgRNA (300 ng/µL), 2 µL Phenol
667 Red for visualisation and nuclease free water up to 10 µL (kept on ice). The needles were pulled from
668 glass capillaries 1.0 OD x 0.58 ID x 100 L mm using a micropipette puller machine with the program
669 previously established in the lab. One- or two-cell stage embryos were placed and fixed in the agarose
670 plate and injected with a small amount of reaction mix directly into the embryos one at a time. The
671 embryos were transferred to the clean methylene blue solution, checked daily and further handled as
672 previously described for embryo maintenance. To genotype CRISPR/Cas9 injected fish and their progeny,
673 first fish DNA had to isolated from 2-4 scales which were collected from the posterior part of the body of
674 sexually matured fish (minimum 5-6 weeks of age). The scales were transferred to 50 µL of SEL buffer
675 (1M KCl, 1M $MgCl_2$, 1M Tris pH 8,3, 10% Igepal, 10% Tween-20, 0,1% Gelatine in miliQ H_2O) and 1
676 µL of Proteinase K. The scales were incubated in the SEL isolation buffer and Proteinase K at 60°C for 1
677 h, 90°C for 15 min and 12°C until tubes were taken out of the machine. The isolated DNA was used as a
678 template for PCR amplification of the target region of interest. *Taq* 2X Master Mix was used for the PCR
679 reaction. PCR details. Forward primer: CCTCTCTTTCAGGTCCCCAC. Reverse primer:

680 TTTTCTGCTCTGCT TTTAGGC. Amplicon Length: 209 bp. CONDITIONS: **(1x)** 3:00 95.0C **(35x)**
681 0:45 95.0C 0:30 55.0C 0:45 72.0C (**1x)** 5:00 68.0 ∞ 10.0 PCR amplicons were purified using Sera-Mag
682 SpeedBead Carboxylate-Modified Magnetic Particles (Hydrophylic) magnetic beads. Purified DNA was
683 sent for Sanger sequencing to the Eurofins Genomics (https://eurofinsgenomics.eu/).
684
685 *Sample preparation for proteomics analysis*
686 Before lysis, lysis buffer (fc 4% SDS, 100 mM HEPES, pH 8.5, 50 mM DTT) was added to each samples.
687 Samples were then boiled at 95°C for 7 min and sonicated using a tweeter. Reduction was followed by
688 alkylation with 200 mM iodoacetamide (IAA, final concentration 15 mM) for 30 min at room temperature
689 in the dark. Samples were acidified with phosphoric acid (final concentration 2.5%), and seven times the
690 sample volume of S-trap binding buffer was added (100 mM TEAB, 90% methanol). Samples were bound
691 on 96-well S-trap micro plate (Protifi) and washed three times with binding buffer. Trypsin in 50 mM
692 TEAB pH 8.5 was added to the samples (1 µg per sample) and incubated for 1 h at 47°C. The samples were
693 eluted in three steps with 50 mM TEAB pH 8.5, elution buffer 1 (0.2% formic acid in water) and elution
694 buffer 2 (50% acetonitrile and 0.2% formic acid). The eluates were dried using a speed vacuum centrifuge
695 (Eppendorf Concentrator Plus, Eppendorf AG, Germany) and stored at -20° C. The samples were loaded
696 on Evotips (Evosep) according to the manufacturer's instructions. In short, Evotips were first washed with
697 Evosep buffer B (acetonitrile, 0.1% formic acid), conditioned with 100% isopropanol and equilibrated with
698 Evosep buffer A. Afterwards, the samples were loaded on the Evotips and washed with Evosep buffer A.
699 The loaded Evotips were topped up with buffer A and stored until the measurement.
700
701 *LC-MS Data independent analysis (DIA)*
702 Peptides were separated using the Evosep One system (Evosep, Odense, Denmark) equipped either with a
703 15 cm x 150 µm i.d. packed with a 3 µm Reprosil-Pur C18 bead column (Evosep Endurance, EV-1109,
704 PepSep, Marslev, Denmark) or with a a 15 cm x 150 µm i.d. packed with a 1.5 µm Reprosil-Pur C18 bead
705 column (Evosep Performance, EV-1137, PepSep, Marslev, Denmark) heated at 45°C with a butterfly sleeve

706 oven (Phoenix S&T, Philadelphia, USA). The samples were run with a pre-programmed proprietary Evosep
707 gradient of 44 min (30 samples per day) using water and 0.1% formic acid and solvent B acetonitrile and
708 0.1% formic acid as solvents. The LC was coupled to an Orbitrap Exploris 480 (Thermo Fisher Scientific,
709 Bremen, Germany) using PepSep Sprayers and a Proxeon nanospray source. The peptides were introduced
710 into the mass spectrometer via a PepSep Emitter 360-µm outer diameter × 20-µm inner diameter, heated at
711 300°C, and a spray voltage of 2 kV was applied. The injection capillary temperature was set at 300°C. The
712 radio frequency ion funnel was set to 30%. For DIA data acquisition with endurance column, full scan mass
713 spectrometry (MS) spectra with a mass range of 350–1650 m/z were acquired in profile mode in the
714 Orbitrap with a resolution of 120,000 FWHM. The default charge state was set to 2+, and the filling time
715 was set at a maximum of 60 ms with a limitation of 3 × 106 ions. DIA scans were acquired with 40 mass
716 window segments of differing widths across the MS1 mass range. Higher collisional dissociation
717 fragmentation (normalized collision energy 29%) was applied, and MS/MS spectra were acquired with a
718 resolution of 30,000 FWHM with a fixed first mass of 200 m/z after accumulation of 1 × 106 ions or after
719 filling time of 45 ms (whichever occurred first). Data were acquired in profile mode. For DIA data
720 acquisition for Performance column, full scan mass spectrometry (MS) spectra with a mass range of 350–
721 1650 m/z were acquired in profile mode in the Orbitrap with a resolution of 120,000 FWHM. The default
722 charge state was set to 2+, and the filling time was set at a maximum of 20 ms with a limitation of 3 × 106
723 ions. DIA scans were acquired with 45 mass window segments of differing widths across the MS1 mass
724 range. Higher collisional dissociation fragmentation (normalized collision energy 30%) was applied, and
725 MS/MS spectra were acquired with a resolution of 30,000 FWHM with a fixed first mass of 200 m/z after
726 accumulation of 1 × 106 ions or after filling time of 45 ms (whichever occurred first). For data acquisition
727 and processing of the raw data, Xcalibur 4.5 (Thermo) and Tune version 4.0 were used.
728
729 *Proteomic data processing*
730 DIA raw data were analysed using the directDIA pipeline in Spectronaut (v.17 and v.18, Biognosysis,
731 Switzerland). The data were searched against an in house species-specific database (*N.furzeri*, 59154

entries, Nfu_20150522, annotation nfurzeri_genebuild_v1.150922) with a list of common contaminants appended (247 entries). The data were searched with the following variable modifications: oxidation (M) and acetyl (protein N-term). A maximum of 2 missed cleavages for trypsin and 5 variable modifications were allowed. The identifications were filtered to satisfy an FDR of 1% at the peptide and protein levels. Relative quantification was performed in Spectronaut for each paired comparison using the replicate samples from each condition. Precursors were percentile filtered at 0.2%. The data (candidate table) and data reports (protein quantities) were then exported, and further data analyses and visualization were performed with R studio using in-house pipelines and scripts. Differentially abundant proteins were defined as having a q-value <0.

Active avoidance test

We assessed the decline in learning ability of treated fish using an active avoidance behavioral test which was developed based on a test previously employed in killifish[39,41]. The setup consisted of two circular compartments connected through a small opening. Fish were acclimatized for 15 minutes in water from their home tank before testing began. A red light served as the conditioned stimulus, followed by air bubbles as the negative stimulus. Fish learned to avoid the negative stimulus by crossing the small opening into the opposite compartment when the red light appeared. The red light was presented for 30 seconds, with bubbles introduced after 15 seconds if the fish had not moved. Trials were counted as 'success' if the fish crossed the hurdle within 15 seconds of the red-light onset (before the introduction of bubbles). The cycle of stimulus, bubbles, and rest repeated 40 times per fish. Each fish underwent the test individually and was sacrificed immediately afterward. The entire test lasted one hour per animal. The water temperature was kept stable between 26.5°C and 28.0°C using a standard aquarium heater, which was important as varying temperatures could impact the performance of the fish.

Hybridizing Chain Reaction

757 Probe pair pools targeting *fos* and *neun* transcripts were generated and validated as previously
758 described[35,90]. The probe sequences can be found in **Table S5**. The selected probe pairs were ordered from
759 Integrated DNA Technologies, Inc. (IDT). The HCR protocol (HCRv3.0) was followed as previously
760 published[91] with adaptations for cryosections as described by Van Houcke et al. (2021)[24]. Cryosections of
761 10um thick were used. The amplification of the signal was done for *fos* transcripts with HCR Amplifier
762 B1, Alexa Fluor 647 and *neun* transcripts with HCR Amplifier B2, Alexa Fluor 546. Imaging was done
763 with the Zeiss Axio Scan.Z1 microscope with a Plan-Apochromat 20x/0.8 M27 objective, Axiocam 506m
764 imaging device and 1x Camera Adapter.
765
766

Acknowledgements

We are thankful to the Core Facility Proteomics, Imaging, Histology & Electron Microscopy, and Next Generation Sequencing at the FLI. We are thankful to the Animal fish Facility of the FLI, with a special mention of Johannes Wilfert, as well as Matthias Werres and Christina Paetzold from the fish facility of the MPI-AGE. We would like to thank the group of Lutgarde Arckens at K.U. Leuven (Belgium), and especially Caroline Zandecki, for the help with setting up the hybridizing chain reaction experiment. We are thankful to the group of Randal Halfmann (Stowers Institute) for the expert advice and help with the interpretation of the data, as well as Mario Baumgart for his help with importing the *appa* mutant line to the FLI. D.E.M. de Bakker was financed by a Rubicon scholarship (452021116) from the Dutch Research Council (NWO) as well as by a research grant from the "Balance of the Microverse" Excellence Cluster from the Friedrich Schiller University in Jena. We acknowledge the contribution of the London Neurogenerative Diseases Brain Bank (which is part of the Brains for Dementia Research network, jointly funded by Alzheimer's Research UK and the Alzheimer's Society) that provided us with the human-derived brain samples utilized in this study. This project was funded by the MPI-AGE and from the FLI in Jena. We would like to thank all the past and current members of the Valenzano lab at the MPI-AGE and at the FLI for their continuous input and support.

Data availability

The produced transcriptomic datasets will be made publicly available at the Gene Expression Omnibus from NCBI. To review GEO accession GSE281018, go to https://www.ncbi.nlm.nih.gov/geo/query/acc.cgi?acc=GSE281018. Enter token *cxybacccdzuzluz* into the box. Proteomics data will be made publicly available at MassIVE, which can be found following the links below. Proteomics data for Young (7 weeks) versus Old (6 months) *N. furzeri* brains: http://massive.ucsd.edu/ProteoSAFe/status.jsp?task=650a5a2e981540359f34b145717d2f7b

Proteomics data for *N. furzeri appa* -/- versus *appa* +/+ brains: http://massive.ucsd.edu/ProteoSAFe/status.jsp?task=e7c08aa99a7a427c8ec6eb2623a9e5ec

Declaration of interests

The authors declare no competing interests.

Author contributions

DdB planned the project, managed, designed, and executed most of the experiments including histology, behavioral analysis, and statistical and bioinformatical analysis, produced the figures, acquired funding, and wrote the manuscript. **MM** generation the appa KO line and histological analysis. Produced supplementary figures (S4-8). **KG** and **YR** performed the Filter Retardation Assay. **SB** performed histology on human samples. **FvB:** performed 22C11 Western Blot and critical contributed to the experimental design and interpretation. **BS** Critically contributed to the experimental design and interpretation. **LA** Assisted **DdB** with brain isolation and immunohistochemistry. **FSS** set up and performed HCR experiments. **OO** ran the AlphaFold model. **MB** supervised the transcriptomic data production and analysis. **EC** supervised the proteomic data production and analysis. **AA** shared resources and provided input on the manuscript. **IM** contributed to the manuscript draft. **AS** helped with project conceptualization and provided the pE11 antibody. **AC** aided with sample acquisition and critically contributed to the manuscript draft. **JK** supervised the biochemical analysis of protein aggregation and critically contributed to the manuscript draft. **DRV** Planned and supervised the project, developed the Bayesian models, wrote the manuscript, and acquired the funding.

Bibliography

1. Wyss-Coray, T. Ageing, neurodegeneration and brain rejuvenation. *Nature* vol. 539 Preprint at https://doi.org/10.1038/nature20411 (2016).
2. Pluvinage, J. V. & Wyss-Coray, T. Systemic factors as mediators of brain homeostasis, ageing and neurodegeneration. *Nat Rev Neurosci* **21**, 93–102 (2020).
3. de Bakker, D. E. M. & Valenzano, D. R. Turquoise killifish: A natural model of age-dependent brain degeneration. *Ageing Res Rev* **90**, (2023).
4. Murphy, M. P. & Levine, H. Alzheimer's Disease and the β-Amyloid Peptide. *J Alzheimers Dis* **19**, 311 (2010).
5. Sehar, U., Rawat, P., Reddy, A. P., Kopel, J. & Reddy, P. H. Amyloid Beta in Aging and Alzheimer's Disease. *Int J Mol Sci* **23**, (2022).
6. Alvarez, J., Alvarez-Illera, P., Santo-Domingo, J., Fonteriz, R. I. & Montero, M. Modeling Alzheimer's Disease in Caenorhabditis elegans. *Biomedicines* **10**, (2022).
7. Gallrein, C. *et al.* Novel amyloid-beta pathology C. elegans model reveals distinct neurons as seeds of pathogenicity. *Prog Neurobiol* **198**, (2021).
8. O'Keefe, L. & Denton, D. Using Drosophila Models of Amyloid Toxicity to Study Autophagy in the Pathogenesis of Alzheimer's Disease. *BioMed Research International* vol. 2018 Preprint at https://doi.org/10.1155/2018/5195416 (2018).
9. Iijima, K. *et al.* Dissecting the pathological effects of human Aβ40 and Aβ42 in Drosophila: A potential model for Alzheimer's disease. *Proc Natl Acad Sci U S A* **101**, 6623–6628 (2004).
10. Forner, S. *et al.* Systematic phenotyping and characterization of the 5xFAD mouse model of Alzheimer's disease. *Scientific Data 2021 8:1* **8**, 1–16 (2021).
11. Yokoyama, M., Kobayashi, H., Tatsumi, L. & Tomita, T. Mouse Models of Alzheimer's Disease. *Front Mol Neurosci* **15**, (2022).
12. Poon, C. H., Wang, Y., Fung, M. L., Zhang, C. & Lim, L. W. Rodent Models of Amyloid-Beta Feature of Alzheimer's Disease: Development and Potential Treatment Implications. *Aging Dis* **11**, 1235 (2020).
13. Zhang, Y., Chen, H., Li, R., Sterling, K. & Song, W. Amyloid β-based therapy for Alzheimer's disease: challenges, successes and future. *Signal Transduction and Targeted Therapy 2023 8:1* **8**, 1–26 (2023).
14. van Dyck, C. H. *et al.* Lecanemab in Early Alzheimer's Disease. *N Engl J Med* (2022) doi:10.1056/NEJMOA2212948/SUPPL_FILE/NEJMOA2212948_APPENDIX.PDF.
15. Cummings, J. Anti-Amyloid Monoclonal Antibodies are Transformative Treatments that Redefine Alzheimer's Disease Therapeutics. *Drugs* **83**, 569–576 (2023).
16. Budd Haeberlein, S. *et al.* Two Randomized Phase 3 Studies of Aducanumab in Early Alzheimer's Disease. *Journal of Prevention of Alzheimer's Disease* **9**, 197–210 (2022).
17. Swanson, C. J. *et al.* A randomized, double-blind, phase 2b proof-of-concept clinical trial in early Alzheimer's disease with lecanemab, an anti-Aβ protofibril antibody. *Alzheimers Res Ther* **13**, (2021).
18. Sevigny, J. *et al.* The antibody aducanumab reduces Aβ plaques in Alzheimer's disease. *Nature 2016 537:7618* **537**, 50–56 (2016).
19. Ruparelia, A. A. *et al.* The African killifish: A short-lived vertebrate model to study the biology of sarcopenia and longevity. *Aging Cell* **23**, e13862 (2024).

867 20. Di Cicco, E., Tozzini, E. T., Rossi, G. & Cellerino, A. The short-lived annual fish
868 Nothobranchius furzeri shows a typical teleost aging process reinforced by high incidence
869 of age-dependent neoplasias. *Exp Gerontol* **46**, 249–256 (2011).
870 21. Reichard, M. *et al.* Lifespan and telomere length variation across populations of wild-
871 derived African killifish. *Mol Ecol* **31**, 5979–5992 (2022).
872 22. Hartmann, N. *et al.* Telomeres shorten while Tert expression increases during ageing of
873 the short-lived fish Nothobranchius furzeri. *Mech Ageing Dev* **130**, 290–296 (2009).
874 23. Wendler, S., Hartmann, N., Hoppe, B. & Englert, C. Age-dependent decline in fin
875 regenerative capacity in the short-lived fish Nothobranchius furzeri. *Aging Cell* **14**,
876 (2015).
877 24. Van houcke, J. *et al.* Aging impairs the essential contributions of non-glial progenitors to
878 neurorepair in the dorsal telencephalon of the Killifish Nothobranchius furzeri. *Aging Cell*
879 **20**, (2021).
880 25. Morabito, G., Ryabova, A. & Valenzano, D. R. Immune aging in annual killifish. *Immun*
881 *Ageing* **21**, 18 (2024).
882 26. Bradshaw, W. J., Poeschla, M., Placzek, A., Kean, S. & Valenzano, D. R. Extensive age-
883 dependent loss of antibody diversity in naturally short-lived turquoise killifish. *Elife* **11**,
884 (2022).
885 27. Morabito, G. *et al.* Spontaneous onset of cellular markers of inflammation and genome
886 instability during aging in the immune niche of the naturally short-lived turquoise killifish
887 (Nothobranchius furzeri). *bioRxiv* 2023.02.06.527346 (2023)
888 doi:10.1101/2023.02.06.527346.
889 28. Kelmer Sacramento, E. *et al.* Reduced proteasome activity in the aging brain results in
890 ribosome stoichiometry loss and aggregation. *Mol Syst Biol* (2020)
891 doi:10.15252/msb.20209596.
892 29. Matsui, H., Kenmochi, N. & Namikawa, K. Age- and α-Synuclein-Dependent
893 Degeneration of Dopamine and Noradrenaline Neurons in the Annual Killifish
894 Nothobranchius furzeri. *Cell Rep* **26**, 1727-1733.e6 (2019).
895 30. Louka, A. *et al.* New lessons on TDP-43 from old N. furzeri killifish. *Aging Cell* **21**,
896 (2022).
897 31. Chen, Y. R. *et al.* Tissue-specific landscape of protein aggregation and quality control in
898 an aging vertebrate. *Dev Cell* **0**, (2024).
899 32. Harel, I. *et al.* Identification of protein aggregates in the aging vertebrate brain with prion-
900 like and phase-separation properties. *Cell Rep* **43**, (2024).
901 33. Di Fraia, D. *et al.* Impaired biogenesis of basic proteins impacts multiple hallmarks of the
902 aging brain. *bioRxiv* (2024) doi:10.1101/2023.07.20.549210.
903 34. Tozzini, E. T., Baumgart, M., Battistoni, G. & Cellerino, A. Adult neurogenesis in the
904 short-lived teleost Nothobranchius furzeri: Localization of neurogenic niches, molecular
905 characterization and effects of aging. *Aging Cell* **11**, 241–251 (2012).
906 35. Vanhunsel, S. *et al.* The killifish visual system as an in vivo model to study brain aging
907 and rejuvenation. *NPJ Aging Mech Dis* **7**, (2021).
908 36. Baumgart, M. *et al.* Longitudinal RNA-Seq Analysis of Vertebrate Aging Identifies
909 Mitochondrial Complex I as a Small-Molecule-Sensitive Modifier of Lifespan. *Cell Syst*
910 **2**, 122–132 (2016).

911 37. Bagnoli, S., Fronte, B., Bibbiani, C., Terzibasi Tozzini, E. & Cellerino, A. Quantification
912 of noradrenergic-, dopaminergic-, and tectal-neurons during aging in the short-lived
913 killifish Nothobranchius furzeri. *Aging Cell* **21**, (2022).
914 38. Terzibasi, E. *et al.* Large differences in aging phenotype between strains of the short-lived
915 annual fish Nothobranchius furzeri. *PLoS One* **3**, (2008).
916 39. Valenzano, D. R. *et al.* Resveratrol prolongs lifespan and retards the onset of age-related
917 markers in a short-lived vertebrate. *Current Biology* **16**, 296–300 (2006).
918 40. McKay, A. *et al.* An automated feeding system for the African killifish reveals effects of
919 dietary restriction on lifespan and allows scalable assessment of associative learning. *Elife*
920 **11**, (2022).
921 41. Valenzano, D. R., Terzibasi, E., Cattaneo, A., Domenici, L. & Cellerino, A. Temperature
922 affects longevity and age-related locomotor and cognitive decay in the short-lived fish:
923 Nothobranchius furzeri. *Aging Cell* **5**, 275–278 (2006).
924 42. Bergmans, S., Raes, L., Moons, L. & De Groef, L. A review on neurodegeneration in the
925 fast-ageing killifish, the first animal model to study the natural occurrence of neuronal cell
926 loss. *Ageing Res Rev* **91**, (2023).
927 43. Scheidt, H. A. *et al.* Pyroglutamate-Modified Amyloid β (11- 40) Fibrils Are More Toxic
928 than Wildtype Fibrils but Structurally Very Similar. *Chemistry - A European Journal* **23**,
929 15834–15838 (2017).
930 44. Bayer, T. A. Pyroglutamate Aβ cascade as drug target in Alzheimer's disease. *Molecular*
931 *Psychiatry 2021 27:4* **27**, 1880–1885 (2021).
932 45. D'Angelo, L. Brain atlas of an emerging teleostean model: Nothobranchius furzeri.
933 *Anatomical Record* **296**, 681–691 (2013).
934 46. Jucker, M. *et al.* Age-related deposition of glia-associated fibrillar material in brains of
935 C57BL/6 mice. *Neuroscience* **60**, 875–889 (1994).
936 47. Jucker, M. *et al.* Age-associated inclusions in normal and transgenic mouse brain. *Science*
937 **255**, 1443–1445 (1992).
938 48. Crowhurst, M. O., Layton, J. & Lieschke, G. Developmental biology of zebrafish myeloid
939 cells. *International Journal of Developmental Biology* (2002)
940 doi:10.1387/IJDB.12141435.
941 49. LaFerla, F. M., Green, K. N. & Oddo, S. Intracellular amyloid-β in Alzheimer's disease.
942 *Nature Reviews Neuroscience 2007 8:7* **8**, 499–509 (2007).
943 50. Wegiel, J. *et al.* Intraneuronal Abeta immunoreactivity is not a predictor of brain
944 amyloidosis-beta or neurofibrillary degeneration. *Acta Neuropathol* **113**, 389–402 (2007).
945 51. Oddo, S., Caccamo, A., Smith, I. F., Green, K. N. & LaFerla, F. M. A Dynamic
946 Relationship between Intracellular and Extracellular Pools of Aβ. *Am J Pathol* **168**, 184
947 (2006).
948 52. Mori, C. *et al.* Intraneuronal Aβ42 accumulation in Down syndrome brain. *Amyloid* **9**, 88–
949 102 (2002).
950 53. Gyure, K. A., Durham, R., Stewart, W. F., Smialek, J. E. & Troncoso, J. C. Intraneuronal
951 abeta-amyloid precedes development of amyloid plaques in Down syndrome. *Arch Pathol*
952 *Lab Med* **125**, 489–492 (2001).
953 54. Lee, J. H. *et al.* Faulty autolysosome acidification in Alzheimer's disease mouse models
954 induces autophagic build-up of Aβ in neurons, yielding senile plaques. *Nature*
955 *Neuroscience 2022 25:6* **25**, 688–701 (2022).

956 55. Sullivan, C. P. *et al.* Pyroglutamate-Aβ 3 and 11 colocalize in amyloid plaques in
957 Alzheimer's disease cerebral cortex with pyroglutamate-Aβ 11 forming the central core.
958 *Neurosci Lett* **505**, 109–112 (2011).
959 56. Xue, C., Lin, T. Y., Chang, D. & Guo, Z. Thioflavin T as an amyloid dye: fibril
960 quantification, optimal concentration and effect on aggregation. *R Soc Open Sci* **4**, (2016).
961 57. Scior, A. *et al.* Complete suppression of Htt fibrilization and disaggregation of Htt fibrils
962 by a trimeric chaperone complex. *EMBO J* **37**, 282–299 (2018).
963 58. Mihaljević, M. *Developing a Model for Studying the Role of Amyloid-Beta in*
964 *Nothobranchius Furzeri (Actinopteri; Cypriniformes) Neurodegeneration*.
965 https://urn.nsk.hr/urn:nbn:hr:217:252651.
966 59. Banote, R. K. *et al.* Amyloid precursor protein-b facilitates cell adhesion during early
967 development in zebrafish. *Sci Rep* **10**, (2020).
968 60. Piront, M. L. & Schmidt, R. Inhibition of long-term memory formation by anti-ependymin
969 antisera after active shock-avoidance learning in goldfish. *Brain Res* **442**, 53–62 (1988).
970 61. Inhibition of memory consolidation by antibodies against cell adhesion molecules after
971 active avoidance conditioning in zebrafish - PubMed.
972 https://pubmed.ncbi.nlm.nih.gov/10235674/.
973 62. Lin, X. *et al.* c-Fos mapping of brain regions activated by multi-modal and electric foot
974 shock stress. *Neurobiol Stress* **8**, 92–102 (2018).
975 63. Lara Aparicio, S. Y. *et al.* Current Opinion on the Use of c-Fos in Neuroscience. *NeuroSci*
976 **3**, 687–702 (2022).
977 64. Calvo, R., Hofmann, M. H. & Schluessel, V. Brain areas activated during visual learning
978 in the cichlid fish Pseudotropheus zebra. *Brain Struct Funct* **228**, 859–873 (2023).
979 65. Rodrigue, K. M., Kennedy, K. M. & Park, D. C. Beta-amyloid deposition and the aging
980 brain. *Neuropsychology Review* vol. 19 436–450 Preprint at
981 https://doi.org/10.1007/s11065-009-9118-x (2009).
982 66. Maloney, J. A. *et al.* Molecular Mechanisms of Alzheimer Disease Protection by the
983 A673T Allele of Amyloid Precursor Protein. *J Biol Chem* **289**, 30990 (2014).
984 67. Jonsson, T. *et al.* A mutation in APP protects against Alzheimer's disease and age-related
985 cognitive decline. *Nature 2012 488:7409* **488**, 96–99 (2012).
986 68. Rohde, S. K. *et al.* Amyloid-Beta Pathology and Cognitive Performance in Centenarians.
987 *JAMA Neurol* **82**, 837–847 (2025).
988 69. Cui, R. *et al.* Relaxed Selection Limits Lifespan by Increasing Mutation Load. *Cell* **178**,
989 385-399.e20 (2019).
990 70. Hartlage-Rübsamen, M. *et al.* Glutaminyl cyclase contributes to the formation of focal and
991 diffuse pyroglutamate (pGlu)-Aβ deposits in hippocampus via distinct cellular
992 mechanisms. *Acta Neuropathol* **121**, 705–719 (2011).
993 71. Wittnam, J. L. *et al.* Pyroglutamate Amyloid β (Aβ) Aggravates Behavioral Deficits in
994 Transgenic Amyloid Mouse Model for Alzheimer Disease. *J Biol Chem* **287**, 8154 (2012).
995 72. Burrinha, T. *et al.* Upregulation of APP endocytosis by neuronal aging drives amyloid-
996 dependent synapse loss. *J Cell Sci* **134**, (2021).
997 73. Huse, J. T. *et al.* β-secretase processing in the trans-Golgi network preferentially generates
998 truncated amyloid species that accumulate in Alzheimer's disease brain. *Journal of*
999 *Biological Chemistry* **277**, 16278–16284 (2002).
1000 74. Lu, L. & Hong, W. From endosomes to the trans-Golgi network. *Semin Cell Dev Biol* **31**,
1001 30–39 (2014).

1002 75. Saimani, U. & Kim, K. Traffic from the endosome towards trans-Golgi network. *Eur J*
1003 *Cell Biol* **96**, 198–205 (2017).
1004 76. He, W. & Barrow, C. J. The A beta 3-pyroglutamyl and 11-pyroglutamyl peptides found
1005 in senile plaque have greater beta-sheet forming and aggregation propensities in vitro than
1006 full-length A beta. *Biochemistry* **38**, 10871–10877 (1999).
1007 77. Luheshi, L. M. *et al.* Sequestration of the Aβ peptide prevents toxicity and promotes
1008 degradation in vivo. *PLoS Biol* **8**, (2010).
1009 78. Wang, S. *et al.* Amyloid β precursor protein regulates neuron survival and maturation in
1010 the adult mouse brain. *Molecular and Cellular Neuroscience* **77**, 21–33 (2016).
1011 79. Zheng, H. *et al.* beta-Amyloid precursor protein-deficient mice show reactive gliosis and
1012 decreased locomotor activity. *Cell* **81**, 525–531 (1995).
1013 80. Senechal, Y., Kelly, P. H. & Dev, K. K. Amyloid precursor protein knockout mice show
1014 age-dependent deficits in passive avoidance learning. *Behavioural Brain Research* **186**,
1015 126–132 (2008).
1016 81. Morley, J. E., Farr, S. A., Nguyen, A. D. & Xu, F. What is the Physiological Function of
1017 Amyloid-Beta Protein? *Journal of Nutrition, Health and Aging* **23**, 225–226 (2019).
1018 82. Glasauer, S. M. K. & Neuhauss, S. C. F. Whole-genome duplication in teleost fishes and
1019 its evolutionary consequences. *Molecular Genetics and Genomics* **289**, 1045–1060 (2014).
1020 83. Naumann, U., Brazzell, J. L., Crim, M. J. & Hoppe, B. Comprehensive Colony Health
1021 Management and Emerging Pathogens of the Annual Killifish Species Nothobranchius
1022 furzeri. *J Am Assoc Lab Anim Sci* **63**, 20–33 (2024).
1023 84. Abramson, J. *et al.* Accurate structure prediction of biomolecular interactions with
1024 AlphaFold 3. *Nature 2024 630:8016* **630**, 493–500 (2024).
1025 85. Pettersen, E. F. *et al.* UCSF ChimeraX: Structure visualization for researchers, educators,
1026 and developers. *Protein Sci* **30**, 70–82 (2021).
1027 86. Bentley, D. R. *et al.* Accurate whole human genome sequencing using reversible
1028 terminator chemistry. *Nature* **456**, 53–59 (2008).
1029 87. Willemsen, D., Cui, R., Reichard, M. & Valenzano, D. R. Intra-species differences in
1030 population size shape life history and genome evolution. *Elife* **9**, 1–26 (2020).
1031 88. Robinson, M. D., McCarthy, D. J. & Smyth, G. K. edgeR: a Bioconductor package for
1032 differential expression analysis of digital gene expression data. *Bioinformatics* **26**, 139–
1033 140 (2010).
1034 89. Huang, D. W., Sherman, B. T. & Lempicki, R. A. Systematic and integrative analysis of
1035 large gene lists using DAVID bioinformatics resources. *Nature Protocols 2009 4:1* **4**, 44–
1036 57 (2008).
1037 90. Elagoz, A. M. *et al.* Optimization of Whole Mount RNA Multiplexed in situ
1038 Hybridization Chain Reaction With Immunohistochemistry, Clearing and Imaging to
1039 Visualize Octopus Embryonic Neurogenesis. *Front Physiol* **13**, 882413 (2022).
1040 91. Choi, H. M. T. *et al.* Third-generation in situ hybridization chain reaction: multiplexed,
1041 quantitative, sensitive, versatile, robust. *Development* **145**, (2018).
1042

1043

1044

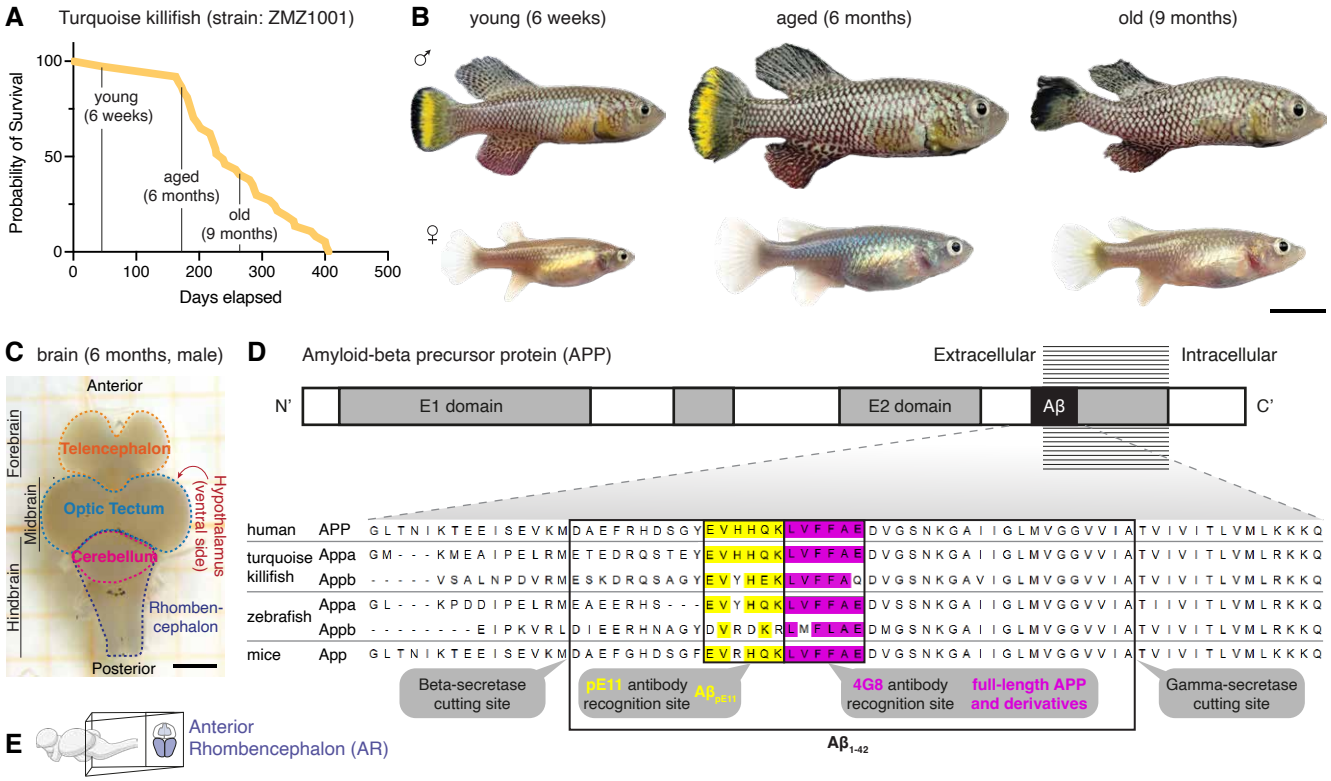

Figure 1. Amyloid-beta precursor protein is evolutionary conserved between turquoise killifish and humans and is expressed in the turquoise killifish brain. (**A**) Survival curve for the turquoise killifish strain ZMZ1001. (**B**) Representative pictures of male and female fish at different ages. Scalebar represents 1 cm. (**C**) Representative brain (6-month-old male) with annotated brain regions. Scalebar represents 1 mm. (**D**) Graphical representation of the amyloid beta precursor protein (APP) and amino acid sequences of APP precursors across four species. Amino acid residues are colored according to their physicochemical properties (ZAPPO): aliphatic/hydrophobic (residues ILVAM) - rose, aromatic (FWY) - orange, positive (KRH) - dark blue, negative (DE) - red, hydrophilic (STNQ) - light green, conformationally special (PG) - magenta, cysteine (C) - yellow. (**E**) Immunohistochemistry staining in the 6-month-old anterior rhombencephalon (AR) using the pE11 and 4G8 antibodies, targeting $A\beta_{pE11-42}$ (yellow) and APP-derivatives (magenta), respectively. Arrowheads indicate $pE11^{+}/4G8^{+}$ signal. Scalebars represent 100 μm in the overview and 25 μm in the zoom-ins.

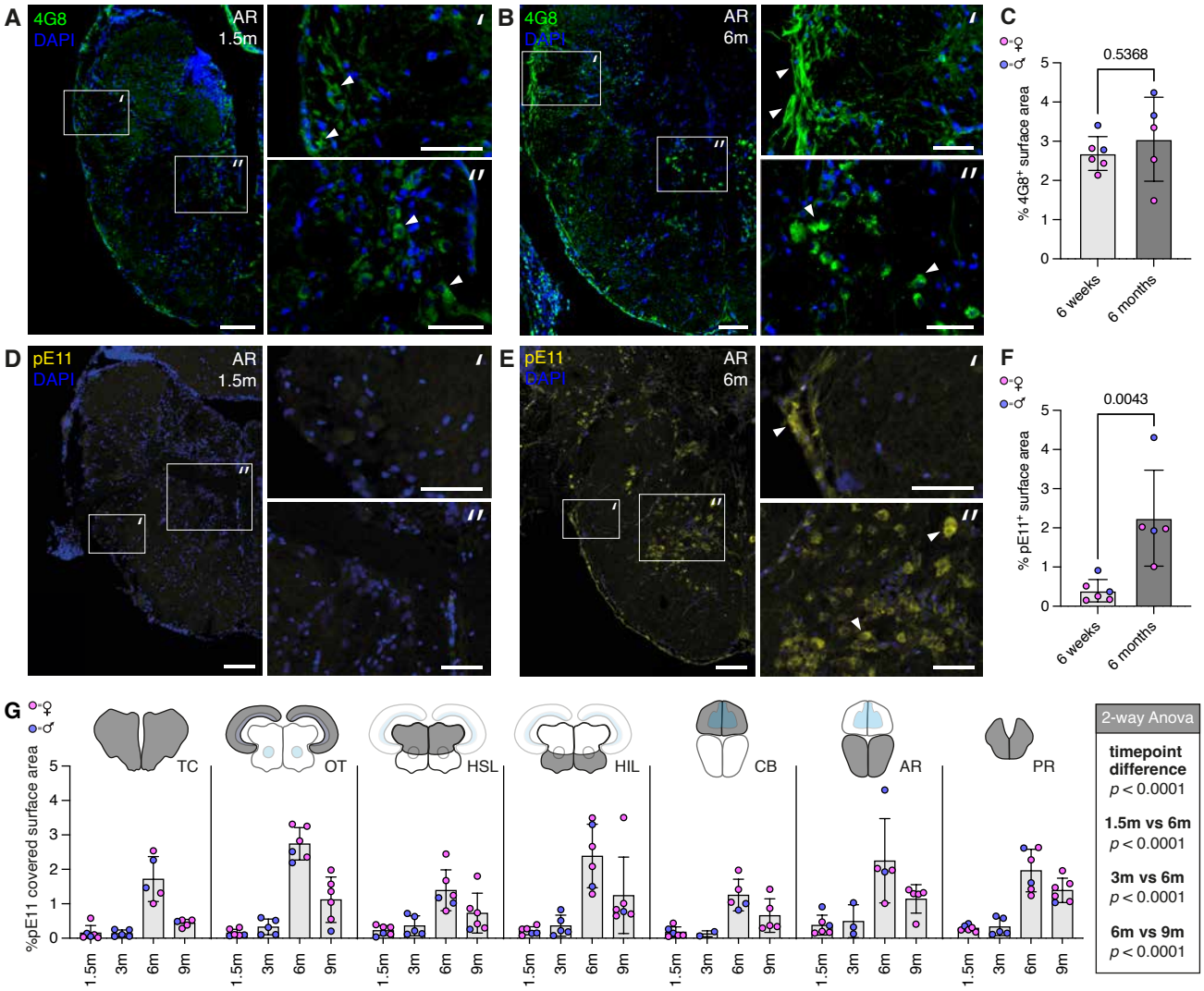

Figure 2. pE11 signal accumulates in an age-dependent manner across the rostro-caudal axis of the turquoise killifish brain. (**A, B**) Immunohistochemistry staining using the 4G8 antibody in the anterior rhombencephalon (AR) of young (6-week-old) and aged (6-month-old) killifish. (**C**) Quantification of the percentage of 4G8-covered surface area in 6-week-old and 6-month-old AR regions. (**D, E**) Immunohistochemistry staining using the pE11 antibody in the anterior rhomboencephalon (AR) of young (6-week-old) and aged (6-month-old) killifish. (**F**) Quantification of the percentage of pE11-covered surface area in 6-week-old and 6-month-old AR regions. (A, B, D, E) Scale bars represent 100 µm in the overview and 50 µm in the zoom-in. Arrowheads indicate positive signal. (C, F) Significance was calculated using a Mann-Whitney test. Error bars represent standard deviation. (**G**) Quantification of the percentage of pE11-covered surface area across seven different brain regions at four different time points, including the telencephalon (TC), optic tectum (OT), hypothalamus superior lobe (HSL), hypothalamus inferior lobe (HIL), cerebellum (CB), anterior rhombencephalon (AR) and posterior rhombencephalon (PR). Error bars represent standard deviation. Significances were calculated using a 2-way Anova test, including a multiple comparison test to investigate the difference between 1.5-months and 6-months, 3-months and 6-months as well as 6-months and 9-months.

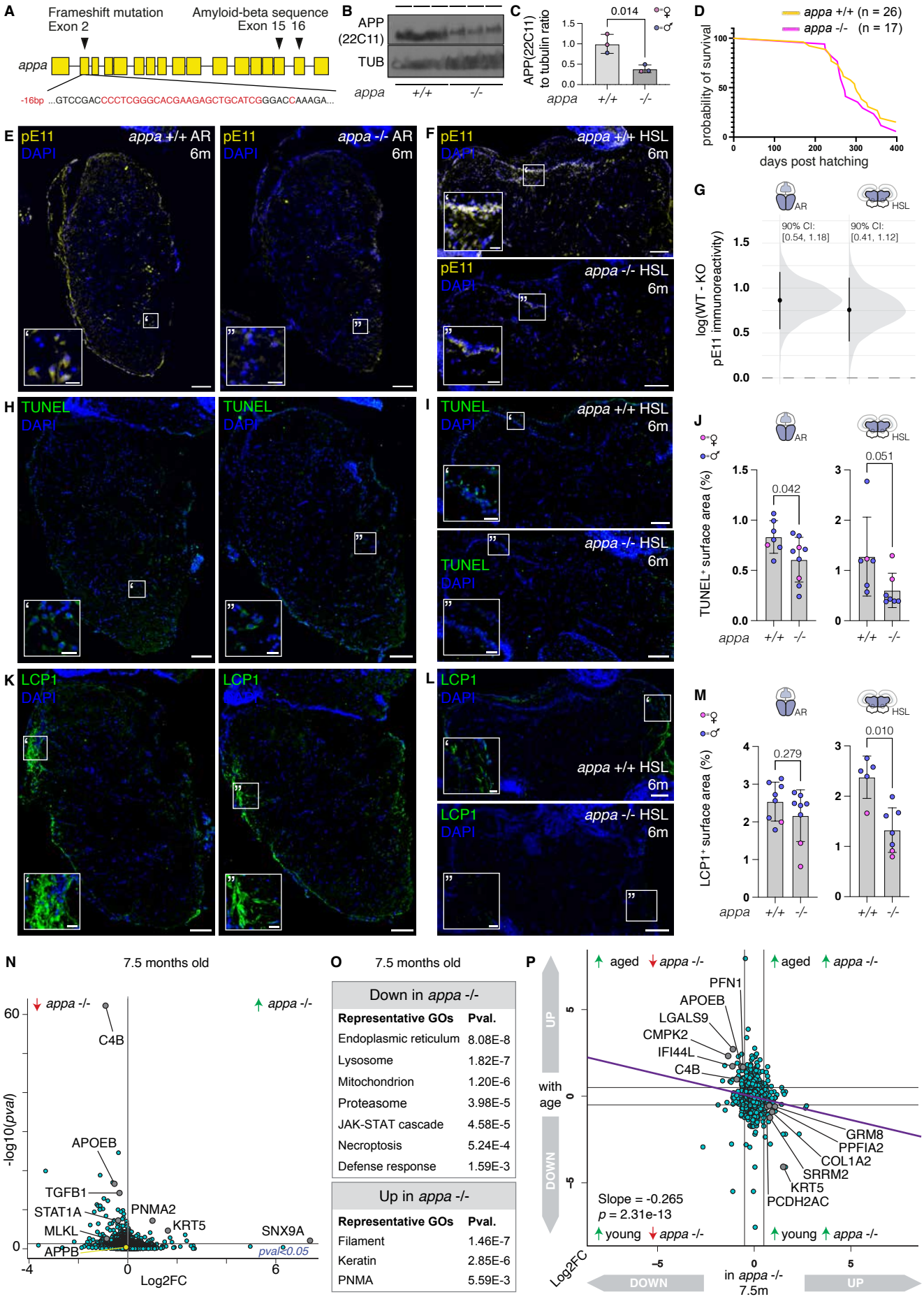
A
Frameshift mutation
Exon 2
Amyloid-beta sequence
Exon 15 16
appa
-16bp ...GTCCGACCCCTCGGGCACGAAGAGCTGCATCGGGACCAAAGA...
B
APP
(22C11)
TUB
appa
+/+
-/-
C
APP(22C11)
to tubulin ratio
0.014
appa
+/+
-/-
D
appa +/+ (n = 26)
appa -/- (n = 17)
probability of survival
days post hatching
E
pE11
DAPI
appa +/+ AR
6m
appa -/- AR
6m
F
appa +/+ HSL
6m
appa -/- HSL
6m
G
AR
HSL
90% CI:
[0.54, 1.18]
90% CI:
[0.41, 1.12]
log(WT - KO
pE11 immunoreactivity)
H
TUNEL
DAPI
I
appa +/+ HSL
6m
appa -/- HSL
6m
J
AR
HSL
0.042
0.051
TUNEL⁺ surface area (%)
appa
+/+
-/-
K
LCP1
DAPI
L
appa +/+ HSL
6m
appa -/- HSL
6m
M
AR
HSL
0.279
0.010
LCP1⁺ surface area (%)
appa
+/+
-/-
N
7.5 months old
appa -/-
appa -/-
C4B
APOEB
TGFB1
STAT1A
PNMA2
MLKL
KRT5
APPB
SNX9A
pval=0.05
-log10(pval)
Log2FC
O
7.5 months old
Down in appa -/-
Representative GOs Pval.
Endoplasmic reticulum 8.08E-8
Lysosome 1.82E-7
Mitochondrion 1.20E-6
Proteasome 3.98E-5
JAK-STAT cascade 4.58E-5
Necroptosis 5.24E-4
Defense response 1.59E-3
Up in appa -/-
Representative GOs Pval.
Filament 1.46E-7
Keratin 2.85E-6
PNMA 5.59E-3
P
aged
appa -/-
aged
appa -/-
PFN1
APOEB
LGALS9
CMPK2
IFI44L
C4B
GRM8
PPFIA2
COL1A2
SRRM2
KRT5
PCDH2AC
with
age
UP
DOWN
Slope = -0.265
p = 2.31e-13
young
appa -/-
young
appa -/-
Log2FC
in appa -/-
7.5m
DOWN
UP

Figure 3. *appa* knock-out mitigates killifish brain aging. (**A**) Schematic representation of the killifish *appa* gene, indicating the mutation site on exon 2, as well as highlighting the location of the amyloid beta coding region in exons 15 and 16. (**B**) Western blot on turquoise killifish lysates from 6-month-old killifish using APP(22C11) and alpha-tubulin targeting antibodies. (**C**) Quantification of western blot results, depicting the APP(22C11) to tubulin ratio. Significance was calculated using a Mann-Whitney test. (**D**) Survival curve of a cohort of wild-type (yellow, n = 26) and *appa* -/- (magenta, n = 17) turquoise killifish of the ZMZ1001 strain. (**E, F**) Representative immunohistochemistry staining results using the pE11 antibody (yellow) in the (E) anterior rhombencephalon (AR) and (F) hypothalamus superior lobe (HSL) of wild-type and *appa* -/- brains. Scale bar represents 100 μm in the overviews and 20 μm in the magnified view. (**G**) Posterior estimates of the genotype effect (WT KO) on pE11 immunoreactivity were obtained using a Bayesian model. Black vertical bars represent the 90% confidence intervals (CIs).The results indicate higher pE11 immunoreactivity in *appa* wild-type (WT) brains compared to *appa* -/- (KO) brains in the anterior rhombencephalon (AR) and hypothalamus superior lobe (HSL) of 6-month-old killifish. (**H, I**) Representative TUNEL staining results (green) in the anterior rhomb-encephalon (AR) and hypothalamus superior lobe (HSL) of wild-type and *appa* -/- brains. (**J**) Quantification of the percentage of TUNEL-covered surface area in anterior rhomboencephalon (AR) and hypothalamus superior lobe (HSL) regions of 6-month-old individuals. Significance was c alculated using a Mann-Whitney test. Error bars represent standard deviation. (**K, L**) Representative immunohistochemistry staining results using the LCP1 antibody (green) in the anterior rhombencephalon (AR) and hypothalamus superior lobe (HSL) of wild-type and *appa* -/- brains. Scale bar represents 100 μm in the overviews and 20 μm in the magnified view. (**M**) Quantification of the percentage of LCP1-cov-ered surface area in anterior rhomboencephalon (AR) and hypothalamus superior lobe (HSL) regions of 6-month-old individuals. Significance was calculated using a Mann-Whitney test. Error bars represent standard deviation. (**N**) Volcano plot displaying differences in brain protein abundance between *appa* -/- mutants and their wild-type siblings (7.5-month-old, 3 males and 3 females per genotype). Differentially abundant proteins are highlighted, representing relevant biological processes. The vertical line indicates log2FC of 0. (**O**) Representative gene ontolo-gies produced from the differentially abundant proteins between 7.5-month-old *appa* -/- mutants and their wild-type siblings (pval < 0.05). (**P**) Proteome-wide comparison between the log2FC of proteins up or downregulated in 6-months-old brains compared to 7-weeks-old brains (y-axis), plotted against the log2FC describing the up and downregulation of proteins in the *appa* mutant compared to the same aged wild-type siblings at 7.5 months.

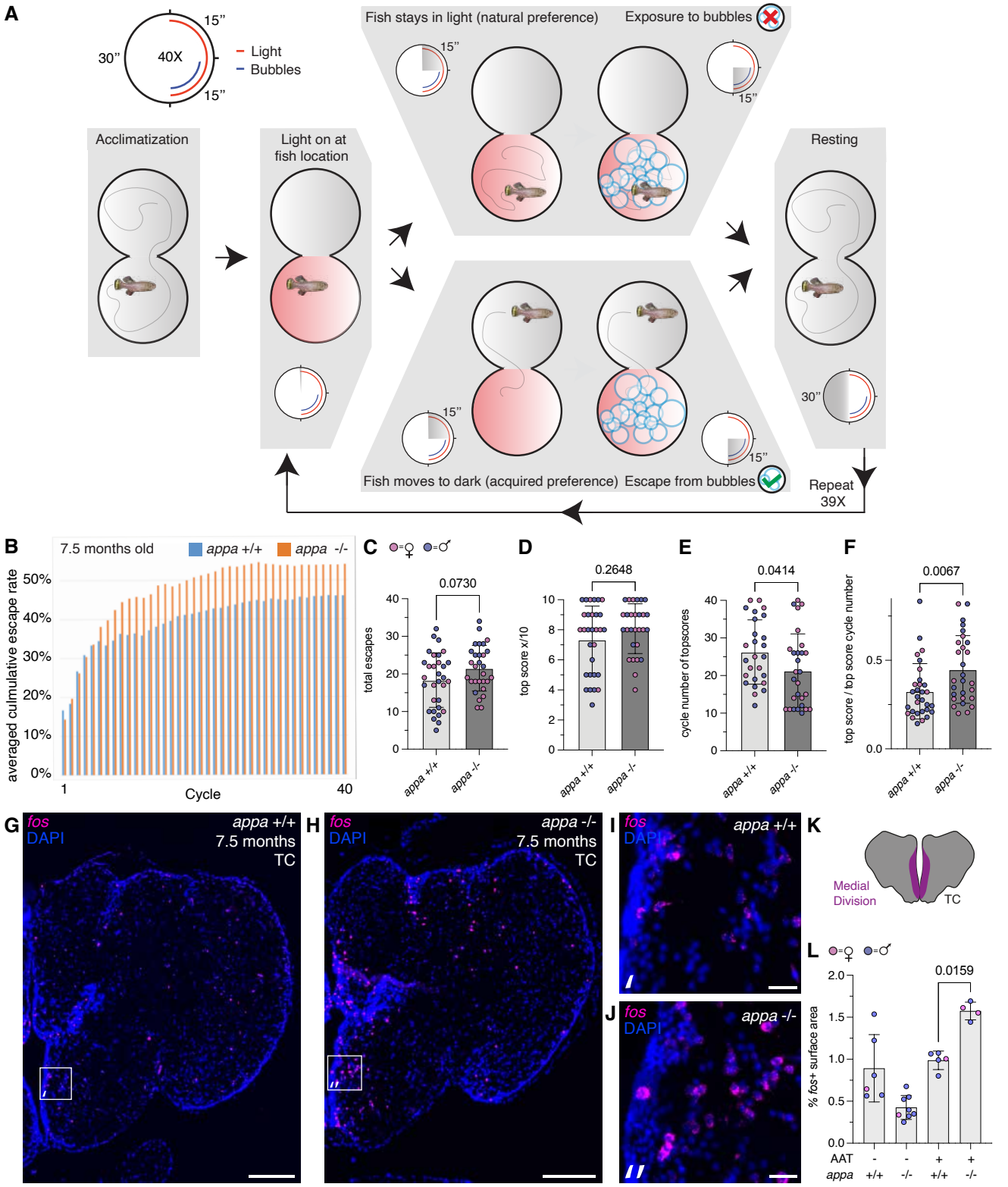

Figure 4. *appa* knock-out mitigates age-related learning deficit in turquoise killifish. (**A**) Experimental set-up of the performed active avoidance test (AAT). (**B**) Plot describing the averaged cumulative escape rate of 7.5-month-old *appa* -/- mutants (orange, n = 28 fish) and their wild-type siblings (blue, n = 30 fish) across 40 cycles. (**C-F**) Quantification of four behavioral traits, compared between 7.5-month-old *appa* -/- mutants and their wild-type siblings. These traits include (**C**) the total escape rate (n/40 cycles), (**D**) the top score of the fish within a window of ten consecutive cycles representing the extent of learning, (**E**) the cycle number at which top scores were reached (excluding non-learners (n=4) defined by total escapes < 10) representing the speed of learning, and (**F**) a combined value in which both the extent and speed of learning were considered (top scores / cycle number at which top scores were reached). Significance values were calculated through Mann-Whitney testing. (**G-J**) Hybridizing Chain Reaction (HCR) staining against *fos* transcripts (magenta), marking neurons involved in active learning within the telencephalon (TC) of *appa* mutants (**H,J**) and their wild-type siblings (**G,I**). Scale bars represent 200 μm in the overview and 20 μm in the zoom-ins. (**K**) Schematic representation of the medial division (magenta) within the telencephalon (TC). (**L**) Quantification of the percentage of *fos*+ surface area in the medial division of the telencephalon of 6-month-old *appa* -/- mutant fish and their wild-type siblings that have not been subjected to an active avoidance test (AAT -), as well as as 7.5-month-old *appa* -/- mutant fish and their wild-type siblings which were subjected to an active avoidance test (AAT +). Significance value was calculated through a Mann-Whitney test.

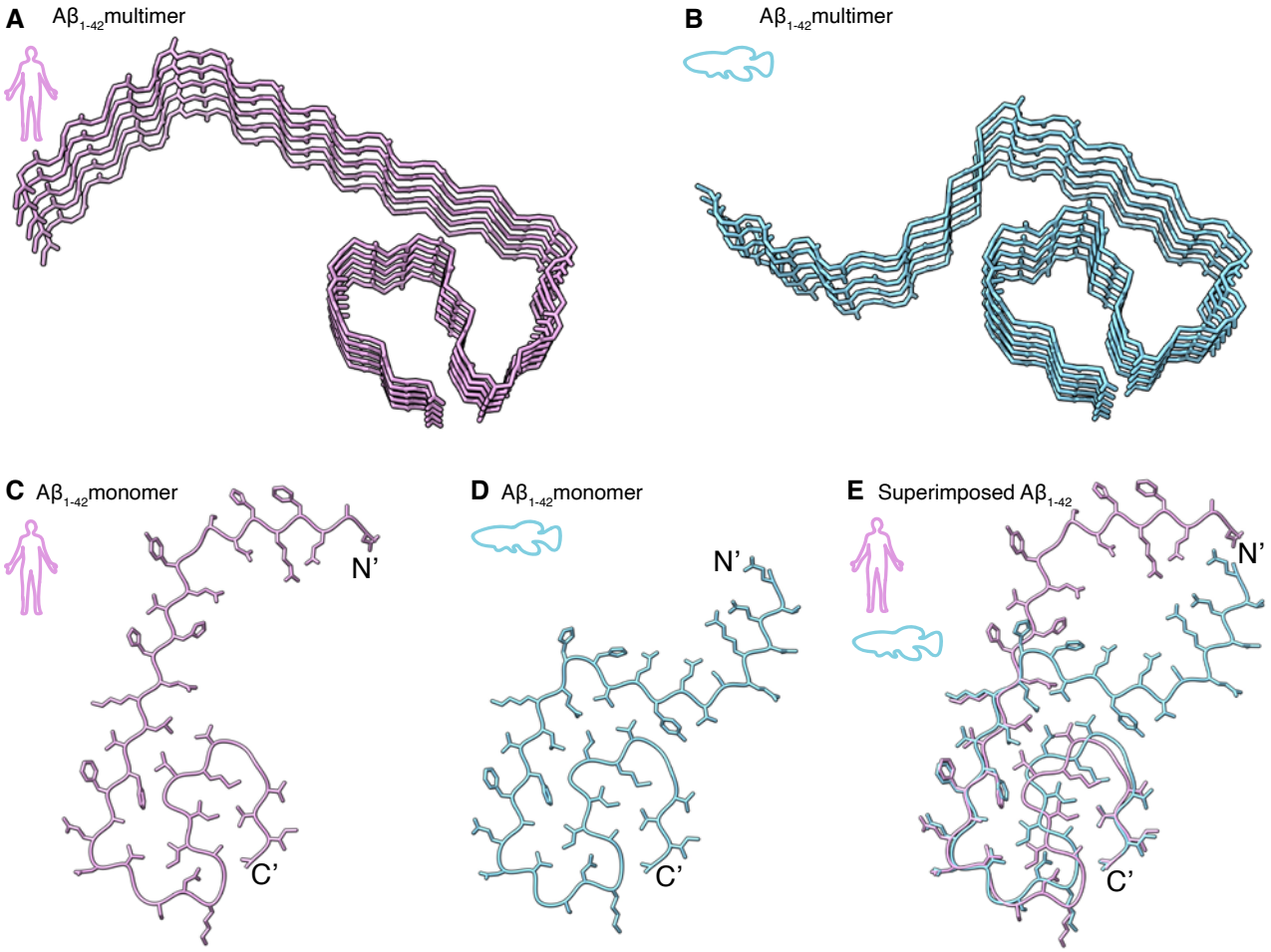

Figure S1. 3D protein structure of amyloid beta (1-42) is conserved between turquoise killifish and humans. (**A**) Alphafold (V3) predicted stucture of human amyloid beta (1-42) in an aggregated state. (**B**) Alphafold-predicted stucture of killifish amyloid beta (1-42) derived from *appa* in an aggregated state. (**C**) Alphafold prediction of human amyloid beta monomer 1-42), as part of the multimer shown in (A). (**D**) Alphafold prediction of turquoise killifish amyloid beta monomer (1-42) derived from *appa*, as part of the multimer shown in (B). (**E**) Superimposed of the Alphafold-predicted multimer structures (only one monomer displayed) of human (pink) and killifish (blue) amyloid beta (1-42) (backbone r.m.s.d. for residues Q15-A42: 0.859 Angstrom).

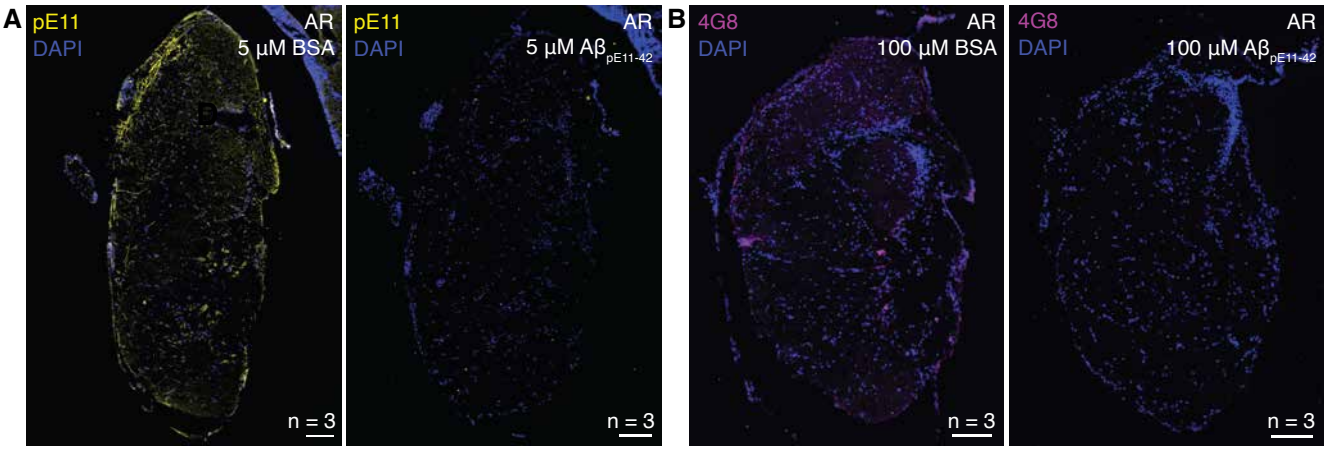

Figure S2. pE11 and 4G8 antibodies bind their targets in an epitope dependent manner. (A-B) Immunohistochemistry staining using the pE11 (A) or 4G8 (B) antibody, after a 30 minute incubation step of the primary antibody together with either BSA (left) or $A\beta_{pE11-42}$ peptide (right). The anterior rhombencephalon (AR) was stained from three 6-month-old turquoise killifish per condition. Scalebars represent 100 μm.

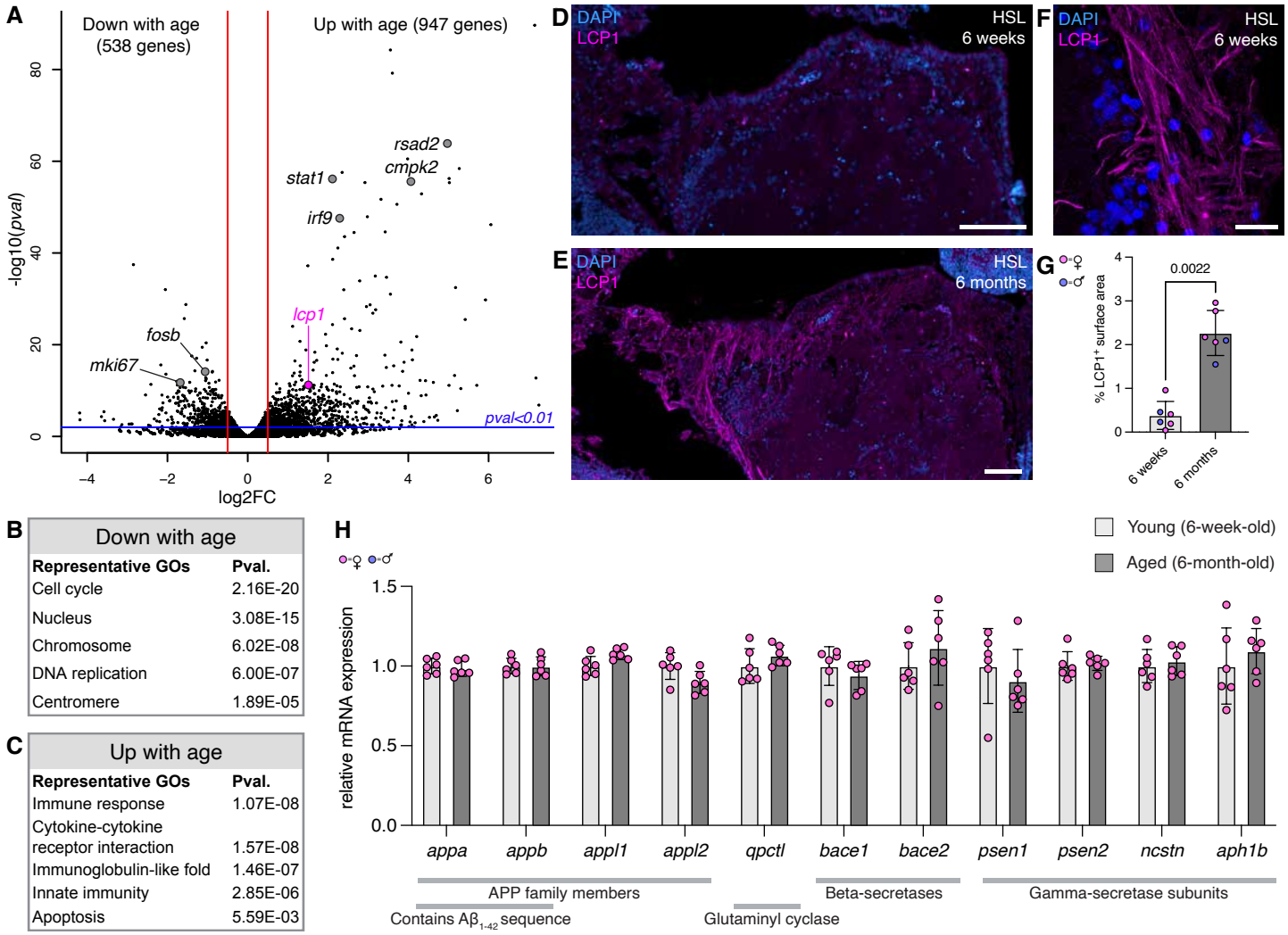

B

Down with age	
Representative GOs	**Pval.**
Cell cycle	2.16E-20
Nucleus	3.08E-15
Chromosome	6.02E-08
DNA replication	6.00E-07
Centromere	1.89E-05

C

Up with age	
Representative GOs	**Pval.**
Immune response	1.07E-08
Cytokine-cytokine receptor interaction	1.57E-08
Immunoglobulin-like fold	1.46E-07
Innate immunity	2.85E-06
Apoptosis	5.59E-03

Figure S3. The turquoise killifish brain develops an age-related inflammatory state while expressing key players of Aβ biogenesis. (**A**) Volcano plot displaying differences in gene expression levels between young (6-week-old) and aged (6-month-old) female killifish brains. Differentially expressed genes are highlighted, representing relevant biological processes. Vertical red lines indicate log2FC of (-)0.5. (**B, C**) Representative gene ontologies produced from the differentially expressed genes between young and old brains (Log2FC > 0.5 / < -0.5 and pval < 0.01). (**D, E**) Immunohistochemistry staining targeting leukocyte marker Lymphocyte Cytosolic Protein 1 (LCP1) in sections of the hypothalamus superior lobe (HSL) from a young (D) and aged (E) individual. Scale bars represent 100 μm. (**F**) High-resolution image of the HSL of a 6-month-old killifish brain, showing the striated pattern of the LCP1 staining, which reflects binding to the actin cytoskeleton. Scale bar represents 20 μm. (**G**) Quantification of the percentage of LCP1+ covered surface area in the hypothalamus of young and aged brains. Significance was calculated using a Mann-Whitney test. Error bars represent standard deviation. (**H**) Expression levels of key players in Aβ biogenesis normalized to total mRNA counts per brain, plotted as relative values to the mean value of young (6-week-old) individuals. APP = Amyloid beta Precursor Protein. Error bars represent standard deviation.

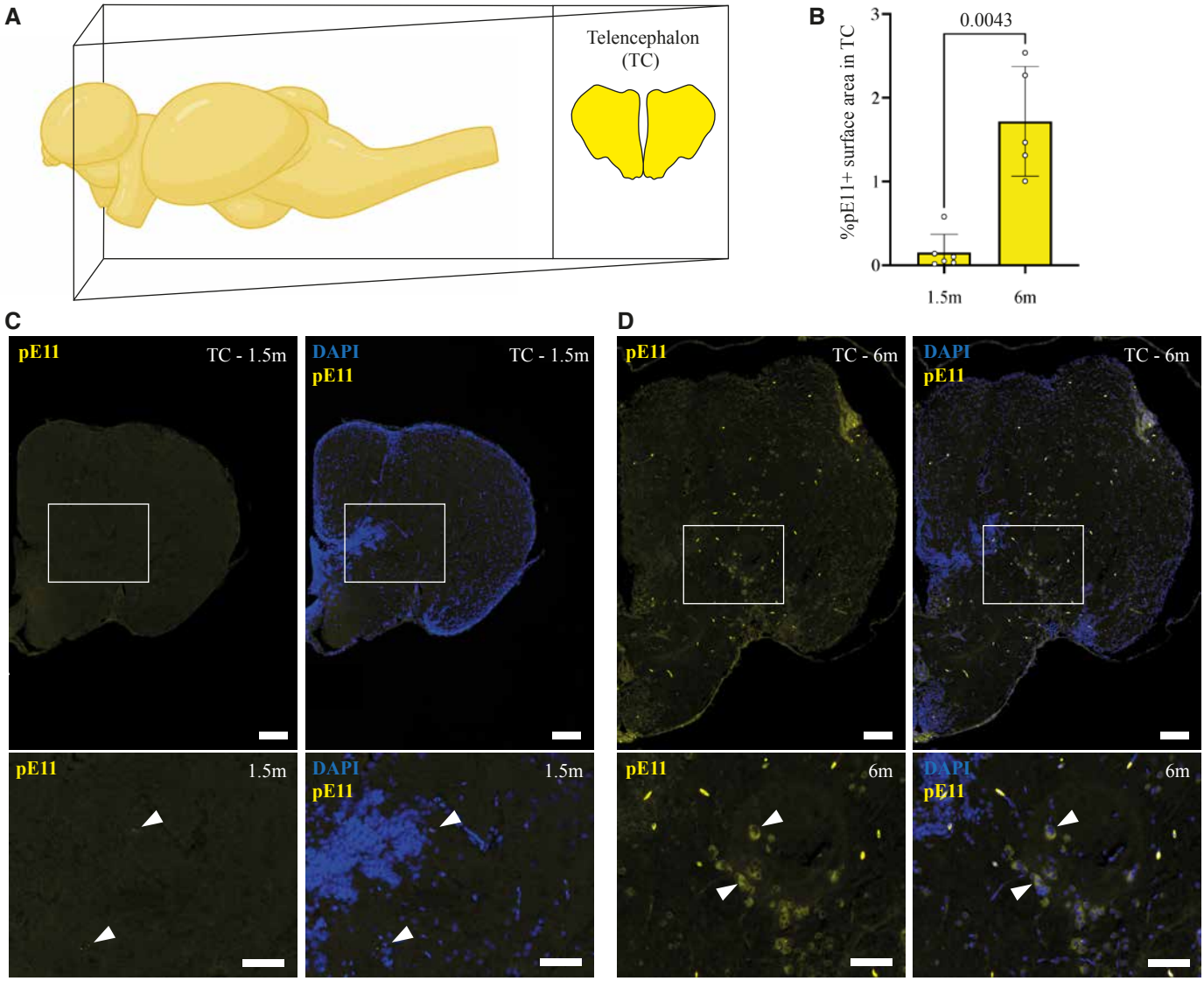

Figure S4. pE11 signal accumulates in the telencephalon in an age-dependent manner. (**A**) Schematic representation of the brain region quantified and shown in B-D. (**B**) Quantification of immunohistochemistry staining using the pE11 antibody on the telencephalon (TC) of young (6-week-old) and aged (6-month-old) killifish. Significance was calculated using a Mann-Whitney test. (**C, D**) Immunohistochemistry staining with the pE11 antibody (yellow) and DAPI (blue) in a 6-week-old (C) and 6-month-old (D) telencephalon. Arrowheads indicate examples of regions with perinuclear immunoreactivity. Scale bar represents 100 μm in the overview and 50 μm in the zoom-in.

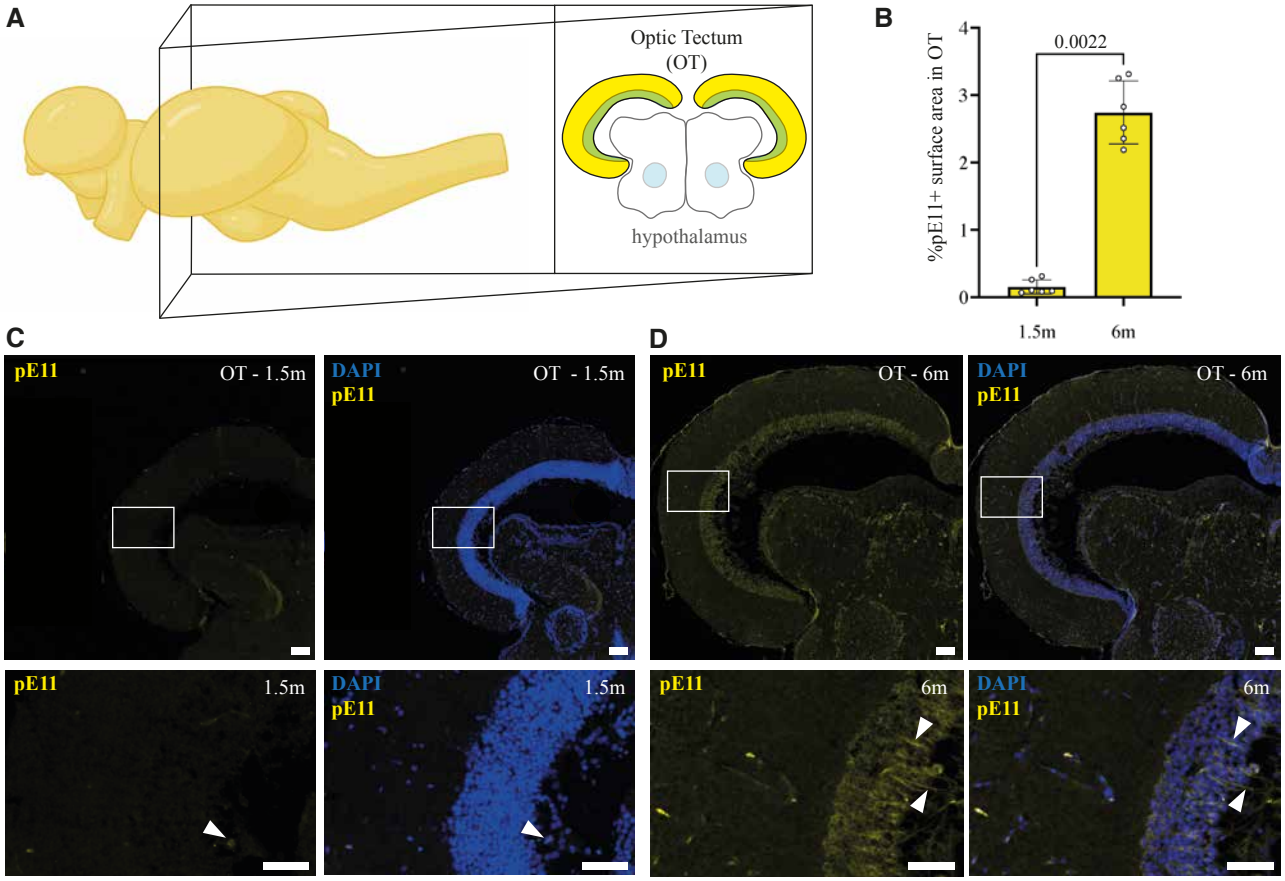

Figure S5. pE11 signal accumulates in the optic tectum in an age-dependent manner. (**A**) Schematic representation of the brain region quantified and shown in B-D. (**B**) Quantification of immunohistochemistry staining using the pE11 antibody on the optic tectum (TC) of young (6-week-old) and aged (6-month-old) killifish. Significance was calculated using a Mann-Whitney test. (**C, D**) Immunohistochemistry staining with the pE11 antibody (yellow) and DAPI (blue) in a 6-week-old (C) and 6-month-old (D) optic tectum. Arrowheads indicate regions with immunoreactivity. Scale bars represent 100 μm in the overviews and 50 μm in the zoom-ins.

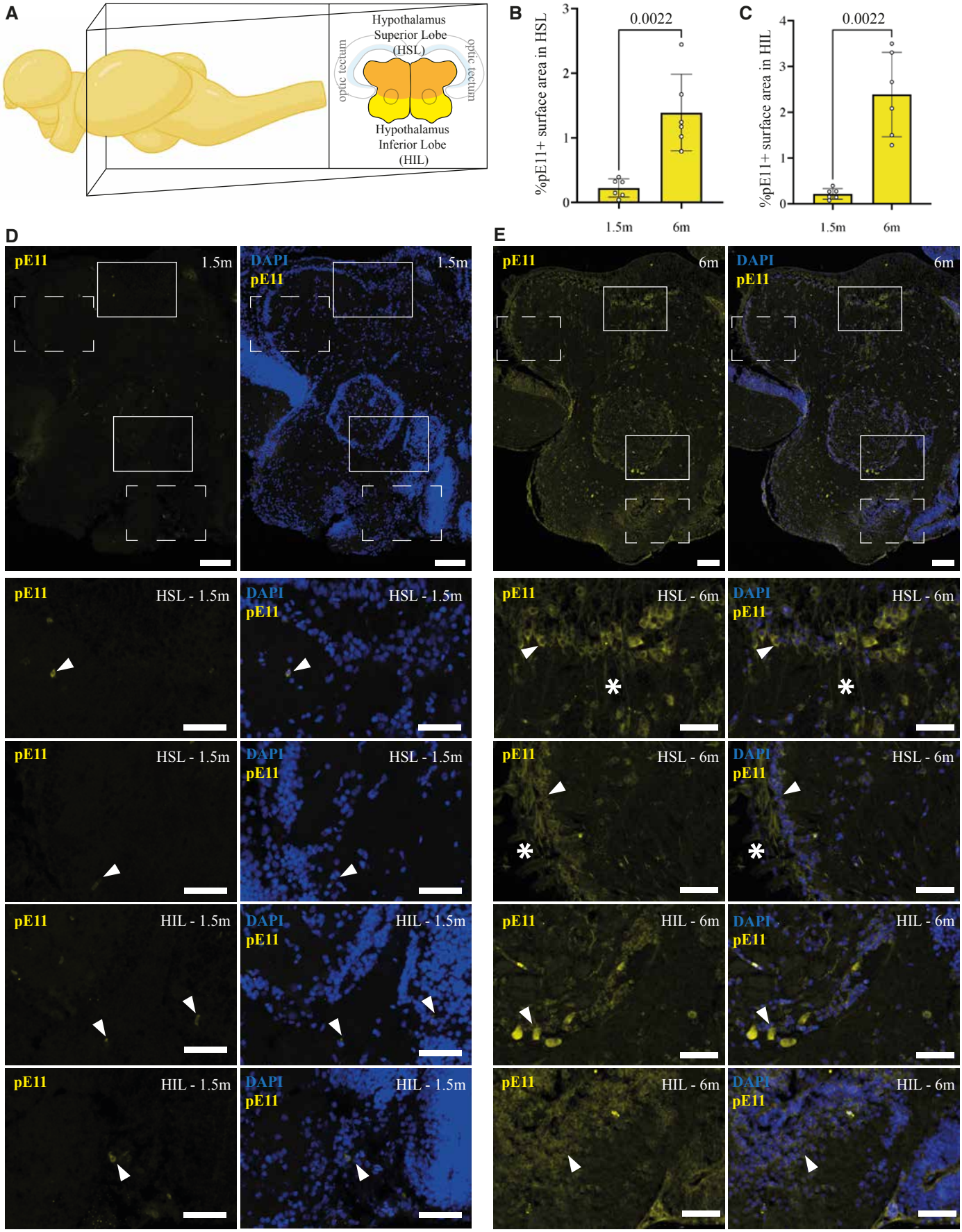

Figure S6. pE11 signal accumulates in the hypothalamus in an age-dependent manner. (**A**) Schematic representation of the brain regions quantified and shown in B-E. (**B,C**) Quantification of immunohistochemistry staining using the pE11 antibody on the hypothalamus superior lobe (HSL) and hypothalamus inferior lobe (HIL) of young (6-week-old) and aged (6-month-old) killifish. Significances were calculated using Mann-Whitney tests. (**D, E**) Immunohistochemistry staining with the pE11 antibody (yellow) and DAPI (blue) in 6-week-old (C) and 6-month-old (D) hypothalamus. Arrowheads indicate regions with perinuclear immunoreactivity. Asterisks indicate regions with filamentous immunoreactivity. Scale bars represent 100 μm in the overviews and 50 μm in the zoom-ins.

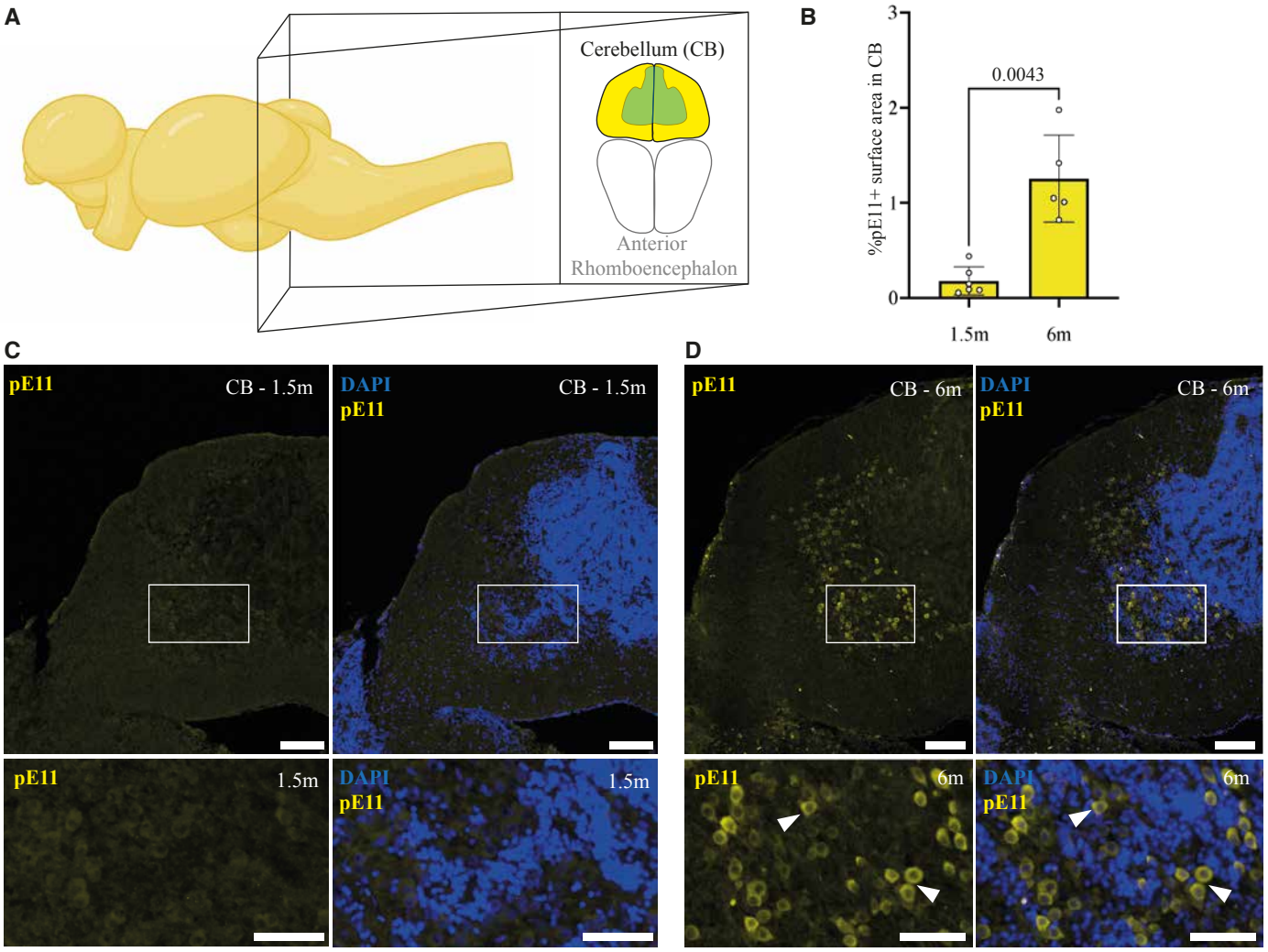

Figure S7. pE11 signal accumulates in the cerebellum in an age-dependent manner. (**A**) Schematic representation of the brain region quantified and shown in B-D. (**B**) Quantification of immunohistochemistry staining using the pE11 antibody on the cerebellum (CB) of young (6-week-old) and aged (6-month-old) killifish. Significance was calculated using a Mann-Whitney test. (**C, D**) Immunohistochemistry staining with the pE11 antibody (yellow) and DAPI (blue) in a 6-week-old (C) and 6-month-old (D) cerebellum. Arrowheads indicate examples of regions with perinuclear immunoreactivity. Scale bars represent 100 μm in the overviews and 50 μm in the zoom-ins.

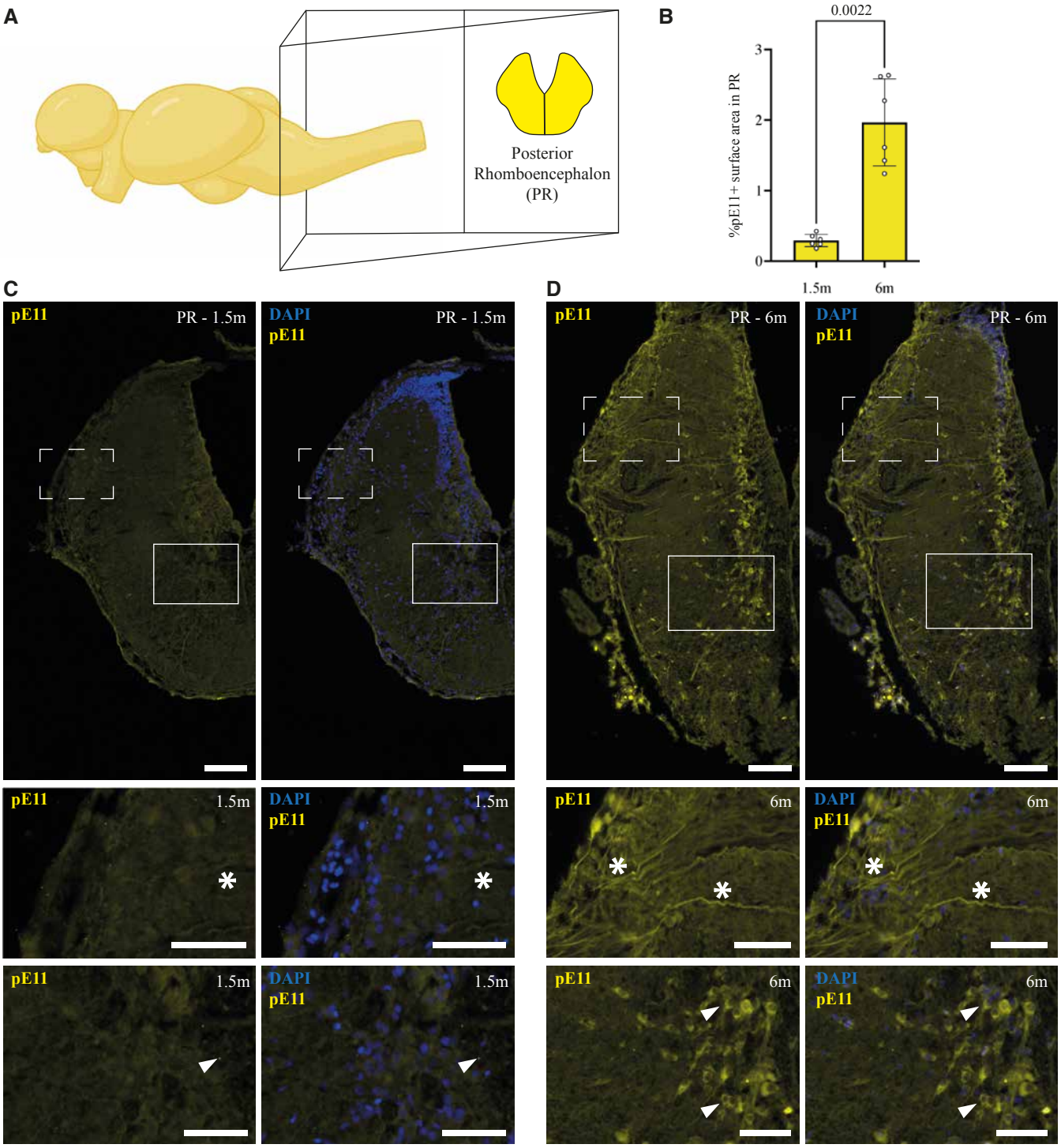

Figure S8. pE11 signal accumulates in the posterior rhomboencephalon in an age-dependent manner. (**A**) Schematic representation of the brain region quantified and shown in B-D. (**B**) Quantification of immunohistochemistry staining using the pE11 antibody on the posterior rhomboencephalon (CB) of young (6-week-old) and aged (6-month-old) killifish. Significance was calculated using a Mann-Whitney test. (**C, D**) Immunohistochemistry staining with the pE11 antibody (yellow) and DAPI (blue) in a 6-week-old (C) and 6-month-old (D) posterior rhomboencephalon. Arrowheads indicate examples of regions with perinuclear immunoreactivity. Asterisks indicate regions with filamentous immunoreactivity. Scale bars represent 100 μm in the overviews and 50 μm in the zoom-ins.

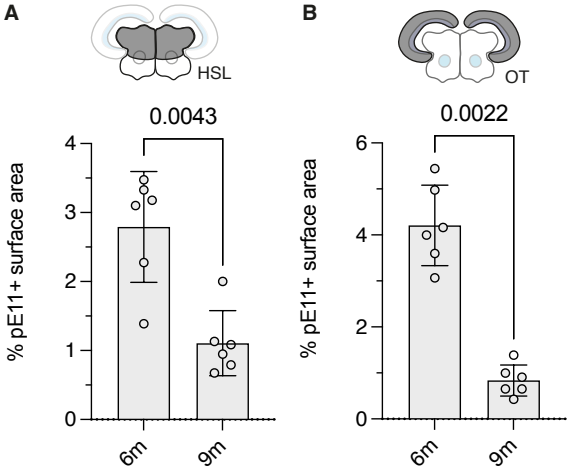

Figure S9. pE11 signal decreases in the turquoise killifish brain between 6- and 9-months of age. (**A, B**) The percentage surface area covered was quantified in an independent cohort of turqoise killifish (strain ZMZ1001) in the (A) hypothalamus superior lobe (HSL) and (B) the optic tetum (OT). Significance was calculated with a Mann-Whitney test.

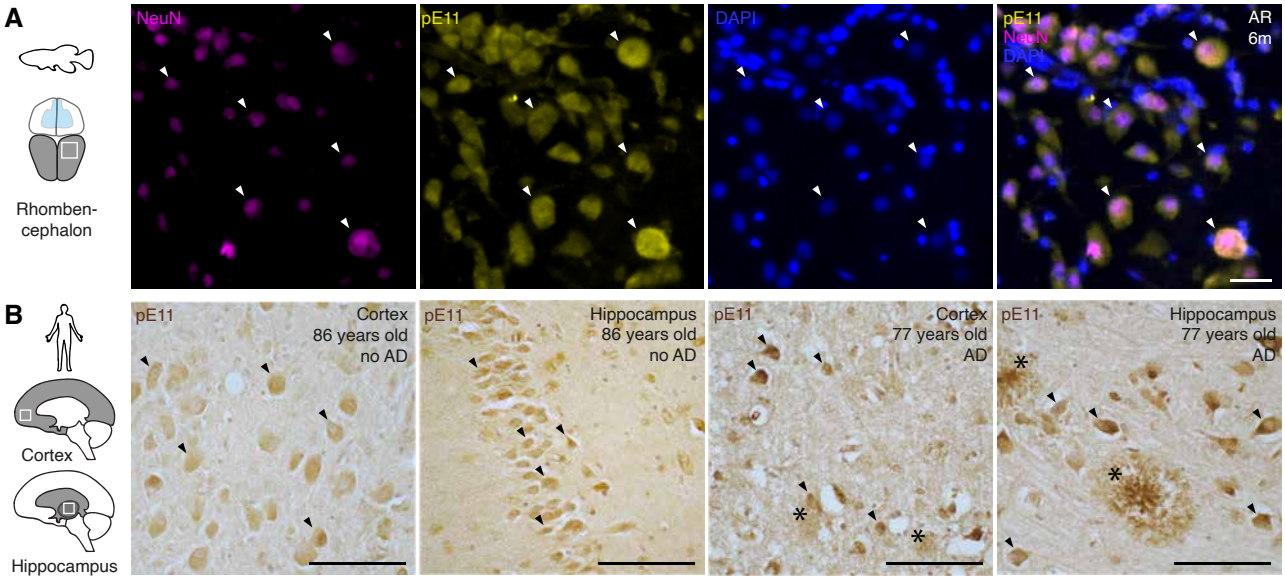

Figure S10. In aged killifish and human brains, pE11 signal predominantly localizes intraneuronally. (**A**) Immunohistochemistry staining in the 6-month-old anterior rhombencephalon (AR) using the pE11 antibody (yellow) and NeuN (Neuronal Nuclei) antibody. Arrowheads indicate colocalizing NeuN and pE11 signals. Scale bar represents 20 μm. (**B**) Immunohistochemistry using the pE11 antibody in two regions of the aged human brain of non-diseased (left) and Alzheimer's diseased (right) brains. Arrowheads indicate intraneuronal signal, the asterisks indicate extracellular plaques. Scale bar represents 100 μm. Images are representative examples of three investigated individuals per condition.

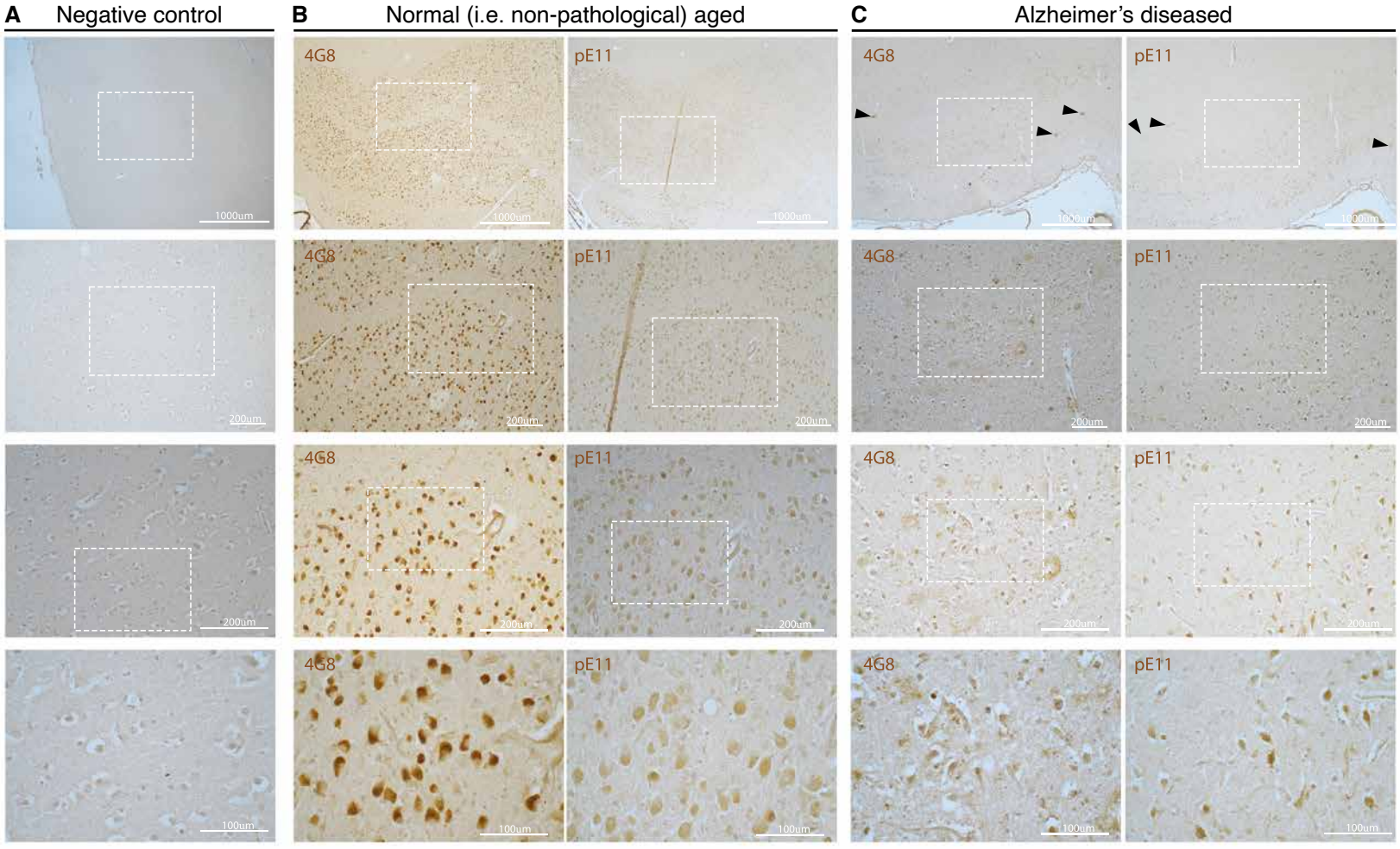

Figure S11. Staining of 4G8 and pE11 in human cortical areas. (**A**) Negative control staining for cortical human areas, realized without the addition of any primary antibody during the protocol. (**B**) Staining for 4G8 and pE11 in cortical areas of a normal (i.e. non-pathological) aged individual (>80 years old). (**C**) Staining for 4G8 and pE11 in cortical areas of an Alzheimer's Disease diagnosed individual (>80 years old). (B, C) These images are representative examples of in total six investigated individuals. Arrowheads indicate extracellular amyloid plaques visualized by 4G8 (left) or pE11 (right).

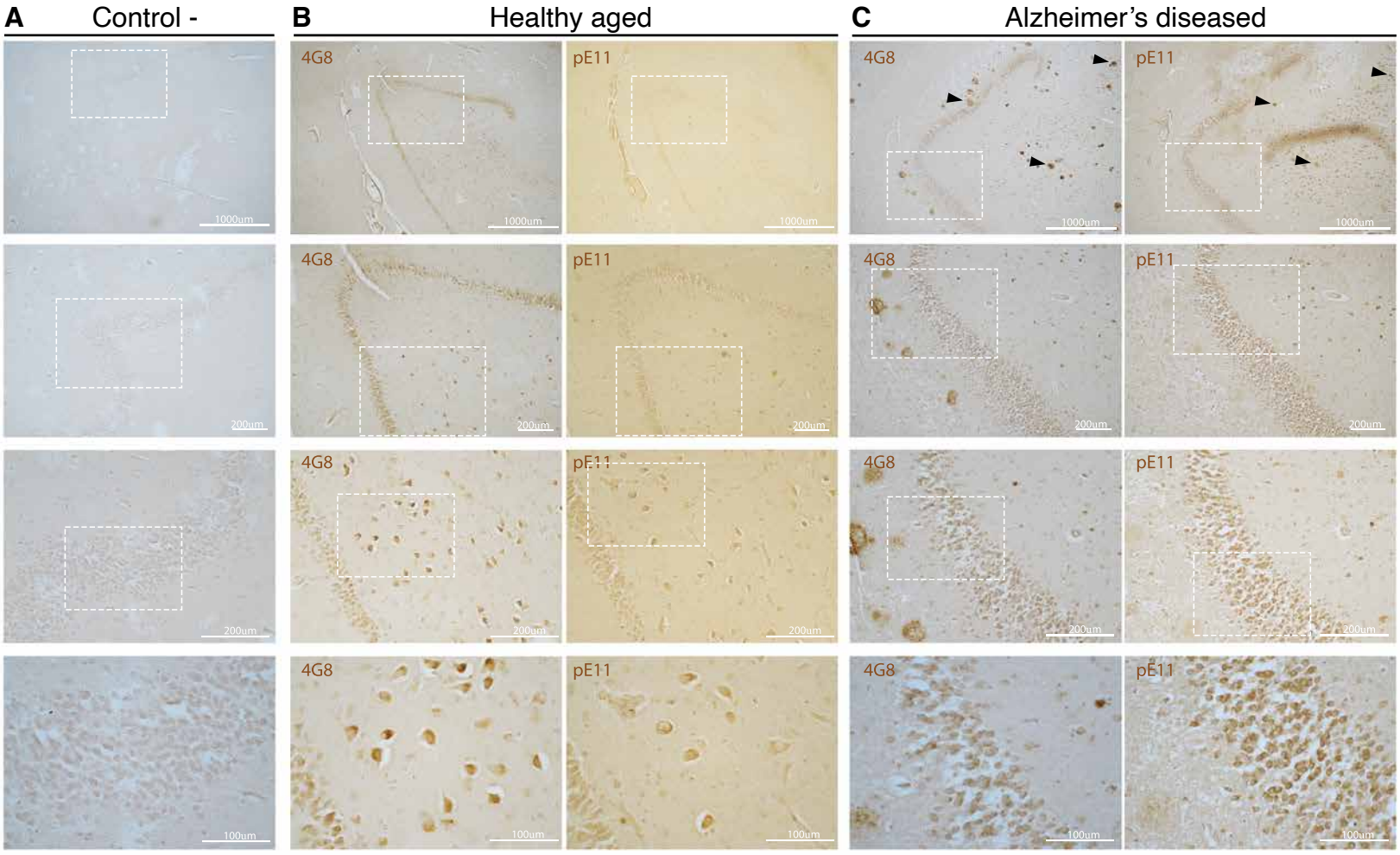

Figure S12. Staining of 4G8 and pE11 in human hippocampus. (**A**) Negative control staining for hippocampal human areas, realized without the addition of any primary antibody during the protocol. (**B**) Staining for 4G8 and pE11 in hippocampal areas of a control patient. (**C**) Staining for 4G8 and pE11 in hippocampal areas of an Alzheimer's Disease affected patient. Arrowheads indicate extracellular amyloid plaques visualized by 4G8 (left) or pE11 (right).

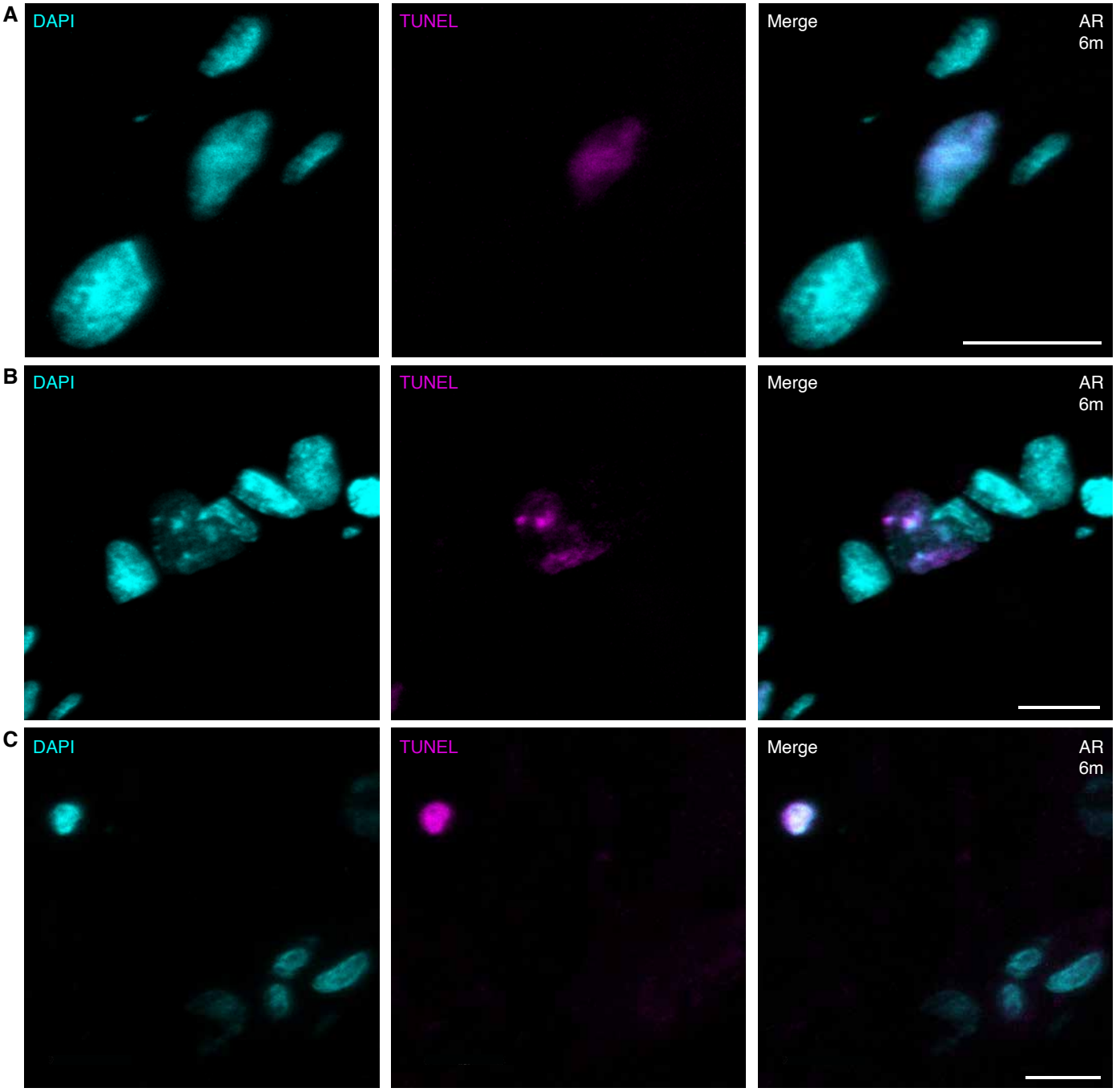

Figure S13. TUNEL staining in the anterior rhombencephalon. (**A-C**) Detection of apoptotic cells in the anterior rhombencephalon (AR) of a 6-month-old turquoise killifish through TUNEL staining. Various staining patterns were identified, including (**A**) visibly intact nuclei, (**B**) fragmented nuclei as well as (**C**) compacted nuclei. Scale bars represent 10 μm. (A-C) All three observed TUNEL staining patterns were observed in three biological replicates.

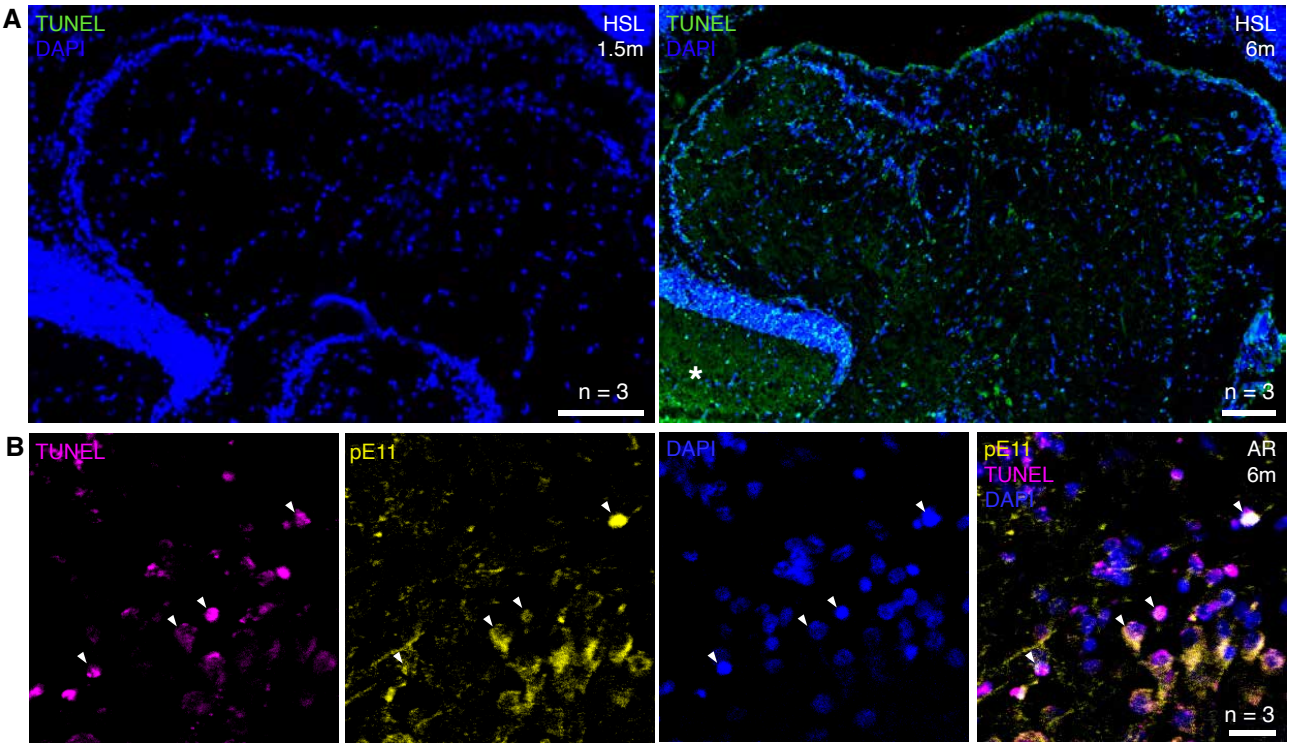

Figure S14. TUNEL staining shows a robust signal in aged turquoise killifish and overlaps with pE11 signal. (**A**) Detection of apoptotic cells in the hypothalamus superior lobe (HSL) of a young 1.5-month-old (**left**) or aged 6-month-old turquoise (**right**) turquoise killifish, visualized through TUNEL staining (green). The asterisk indicates age-related background signal, which was consistent throughout the apical tip of the optic tectum throughout the investigated brain sections of 6-month-old fish. Scale bars represent 100 μm. (**B**) Immunohistochemistry staining using the pE11 antibody (yellow) combined with TUNEL staining (magenta). Arrowheads indicate colocalizing signal. Scale bar represents 20 μm. AR = anterior rhomencephalon.

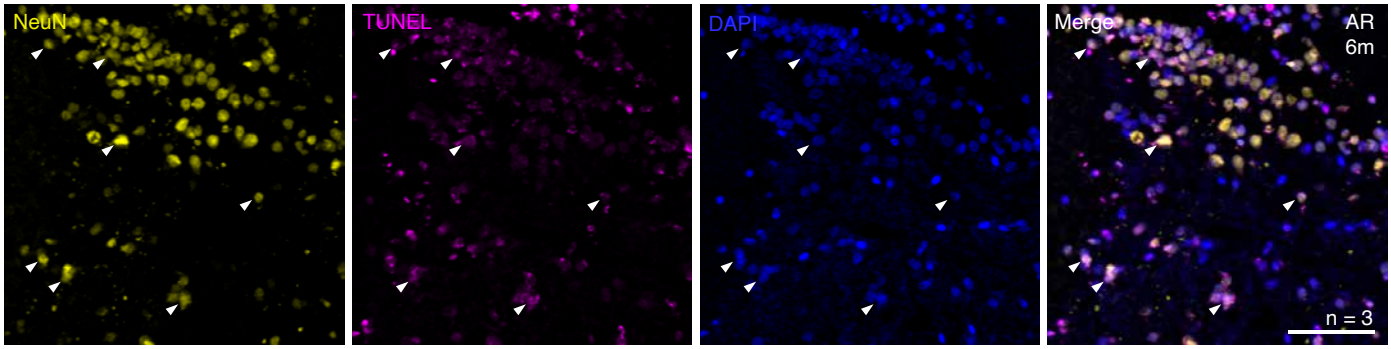

Figure S15. TUNEL staining colocalizes with NeuN in the aged anterior rhombencephalon of the turquoise killifish. (**A**) Immunohistochemistry staining using the pE11 antibody (yellow) combined with TUNEL staining (magenta). Arrowheads indicate colocalizing signal. Scale bar represents 20 μm. The staining was performed on the anterior rhombencephalon (AR) of a 6-month-old turquoise killifish and forms a representative example of three biological replicates.

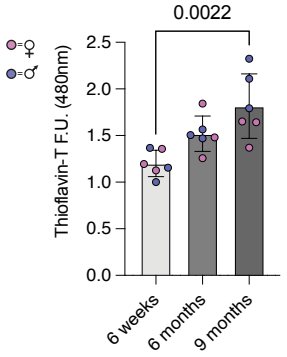

Figure S16. Beta-sheet aggregates accumulate in an age-dependent manner. Thioflavin-T assays were conducted on brain lysates of young, aged and old killifish. Shown values are 480nm emission levels 3 minutes after addition of Thioflavin-T to brain lysates. Values were normalized against the lowest measured value. Significance was calculated using a Mann-Whitney test.

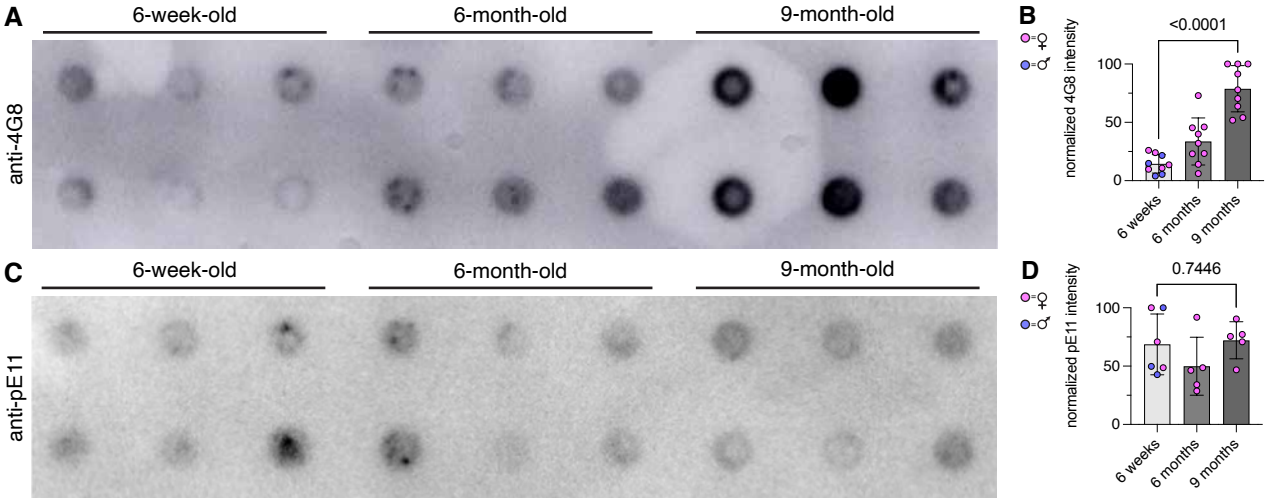

Figure S17. 4G8⁺ peptides aggregate in the turquoise killifish brain in an age-dependent manner. (**A**) Filter retardation analysis of 4G8⁺ aggregates. 100 μg of protein from brain lysates from three individual killifish of each age group was spotted on the filter in duplicates (top/bottom) and probed with an anti-4G8 antibody. (**B**) Quantification of 4G8⁺ signal normalized against the maximum value measured per experiment. Each dot represents the averaged value of three technical replicates per brain. Error bars represent standard deviation. Significance was calculated using a Mann-Whitney test. (**C**) Filter retardation analysis of pE11⁺ aggregates. 100 μg of protein from brain lysates from three individual killifish of each age group was spotted on the filter in duplicates (top/bottom) and probed with an anti-pE11 antibody. (**D**) Quantification of pE11⁺ signal normalized against the maximum value measured per experiment. Each dot represents the averaged value of three technical replicates per brain. Error bars represent standard deviation. Significance was calculated using a Mann-Whitney test.

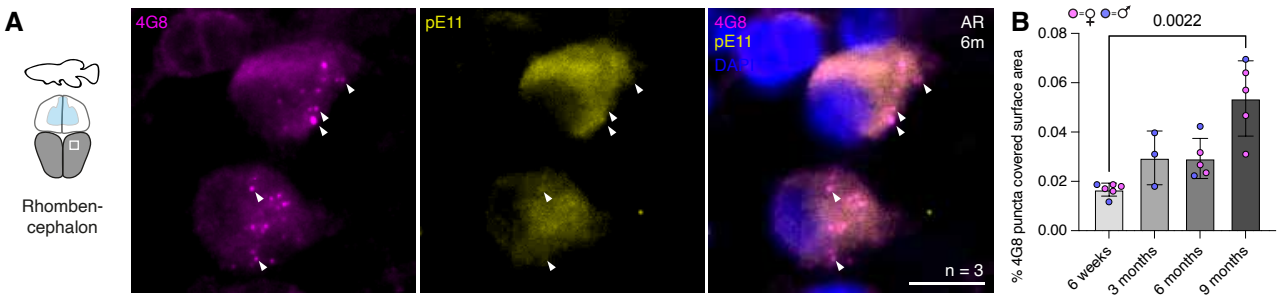

Figure S18. Intraneuronal 4G8⁺/pE11⁻ puncta increase with age in the turquoise killifish brain. (**A**) Immunohistochemistry staining in the 6-month-old anterior rhombencephalon (AR) using the pE11 antibody (yellow) and 4G8 antibody (magenta). Arrowheads indicate 4G8⁺/pE11⁻ puncta. Scale bar represents 10 μm. (**B**) Quantification of the percentage of 4G8⁺-puncta-covered surface area in AR regions at four different ages. Significance was calculated using a Mann-Whitney test. Error bars represent standard deviation.

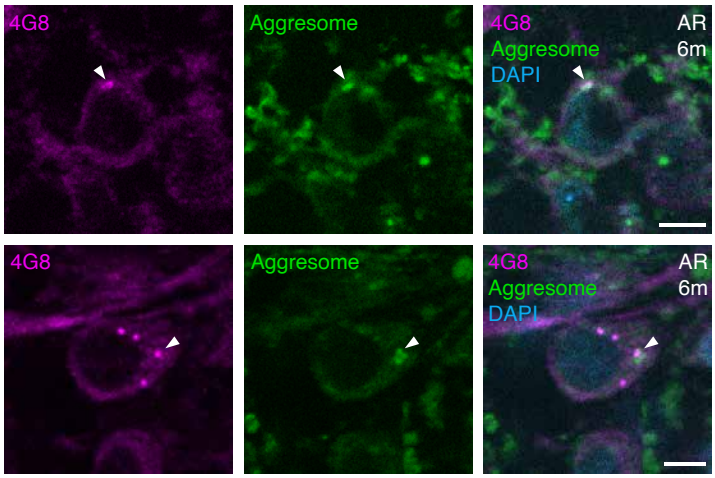

Figure S19. 4G8 puncta partially overlap with Aggresome dye. Two examples of cells in the 6-month-old anterior rhombencephalon (AR) showing an overlap between the 4G8 antibody (magenta) and the PROTEOSTAT Aggresome dye indicating protein aggregates (green). Arrowheads indicate colocalization of Aggresome and 4G8 signal. Scale bars represents 5 μm.

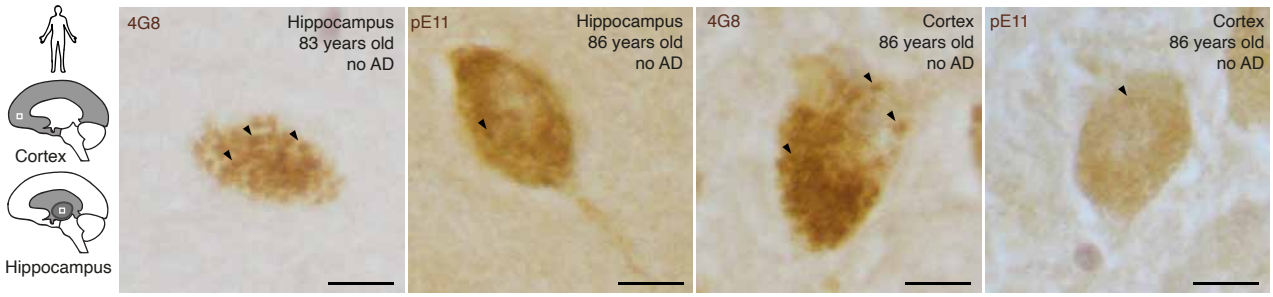

Figure S20. 4G8 staining shows a granulated pattern, which is largely absent in the pE11 staining. Immunohistochemistry using the 4G8 and pE11 antibody in two regions of the non-diseased aged human brain. Arrowheads indicate intraneuronal puncta. Scale bar represents 10 μm.

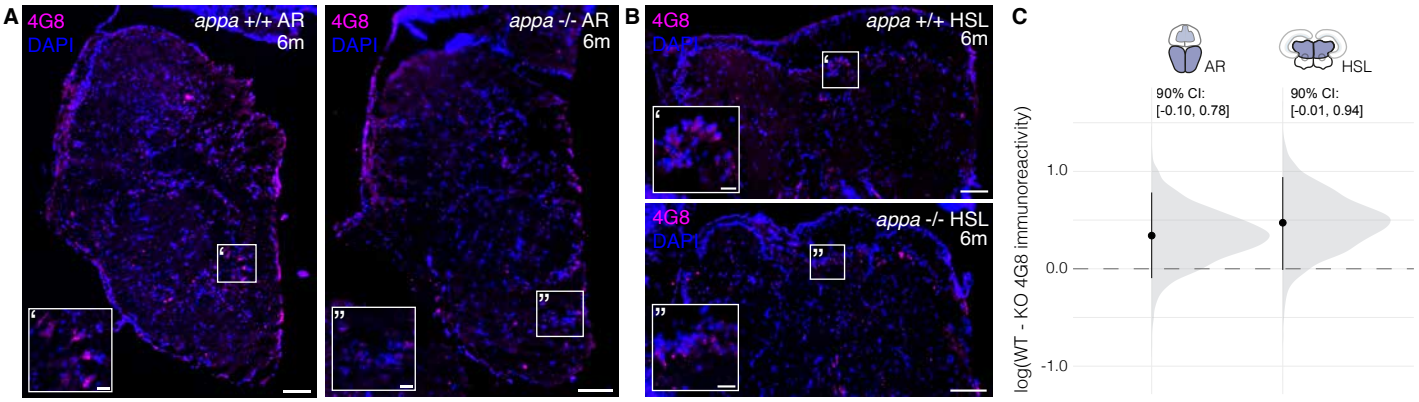

Figure S21. *appa* knock-out reduces 4G8 signal. (**A, B**) Representative immunohistochemistry staining results using the 4G8 antibody (magenta) in the anterior rhombencephalon (AR) of wild-type (A) and *appa* -/- mutant (B) brains. Scale bars represents 100 μm. (**C**) Posterior estimates of the genotype effect (WT – KO) on 4G8 immunoreactivity were obtained using a Bayesian model. Black vertical bars represent the 90% confidence intervals (CIs). The results indicate higher 4G8 immunoreactivity in *appa* wild-type (WT) brains compared to *appa* -/- (KO) brains in the anterior rhombencephalon (AR) and hypothalamus superior lobe (HSL) of 6-month-old killifish.

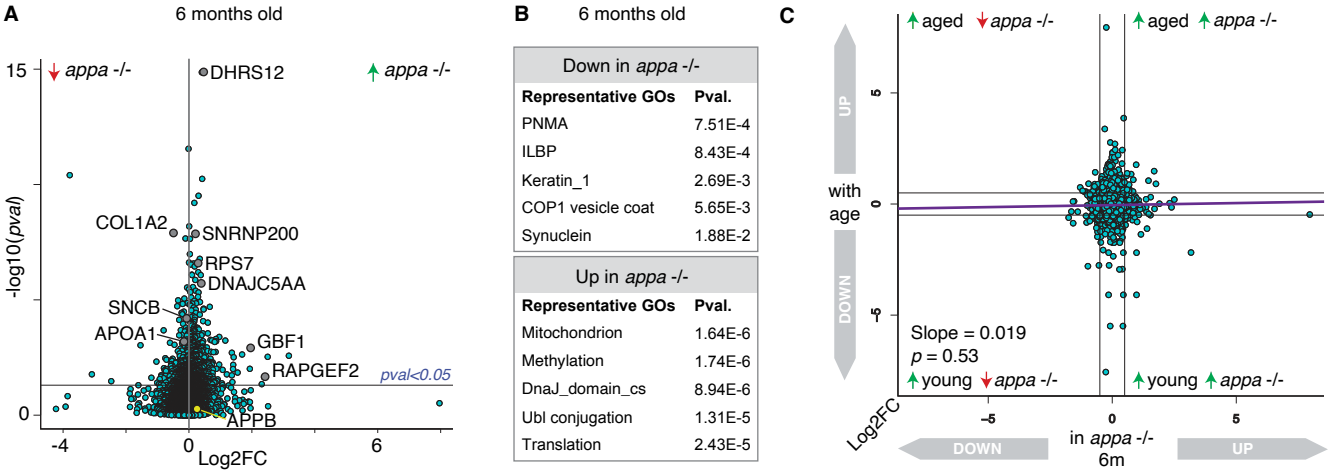

Figure S22. *appa* knock-out affects protein abundances at 6-months of age. (**A**) Volcano plot displaying differences in brain protein abundance between *appa* -/- mutants and their wild-type siblings (6-month-old, 3 males and 3 females per genotype). Differentially abundant proteins are highlighted, representing relevant biological processes. The vertical line indicates log2FC of 0. (**B**) Representative gene ontologies produced from the differentially abundant proteins between 6-month-old *appa* -/- mutants and their wild-type siblings (pval < 0.05). (**C**) Proteome-wide comparison between the log2FC of proteins up or downregulated in 6-months-old brains compared to 7-weeks-old brains (y-axis), plotted against the log2FC describing the up and downregulation of proteins in the *appa* mutant compared to the same aged wild-type siblings at 6 months.

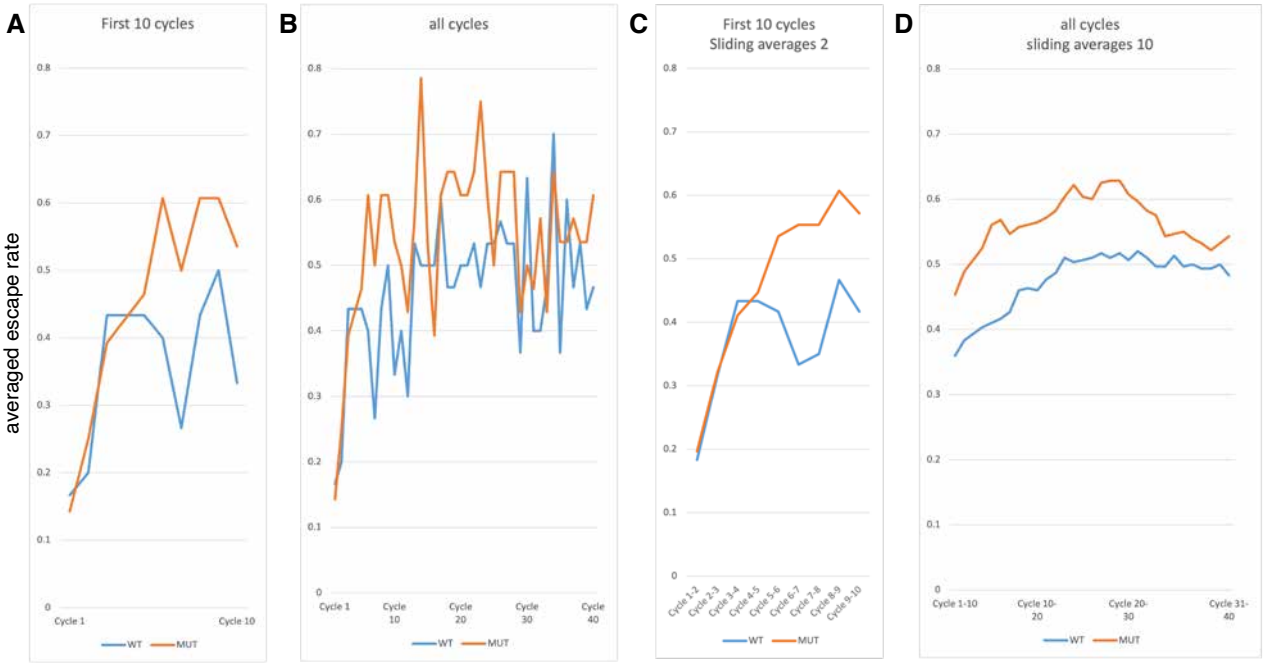

Figure S23. Averaged escape rates of *appa* -/- mutants and their wild-type siblings. (**A, B**) Plot describing the averaged escape rate of 7.5-month-old *appa* -/- mutants (orange, n = 28 fish) and their wild-type siblings (blue, n = 30 fish) across 10 (A) and the full 40 (B) cycles. (**C, D**) Sliding averaged values of the data presented in A and B, using either a sliding average of two (C) or ten (D) to increase the visibility of the general trends.

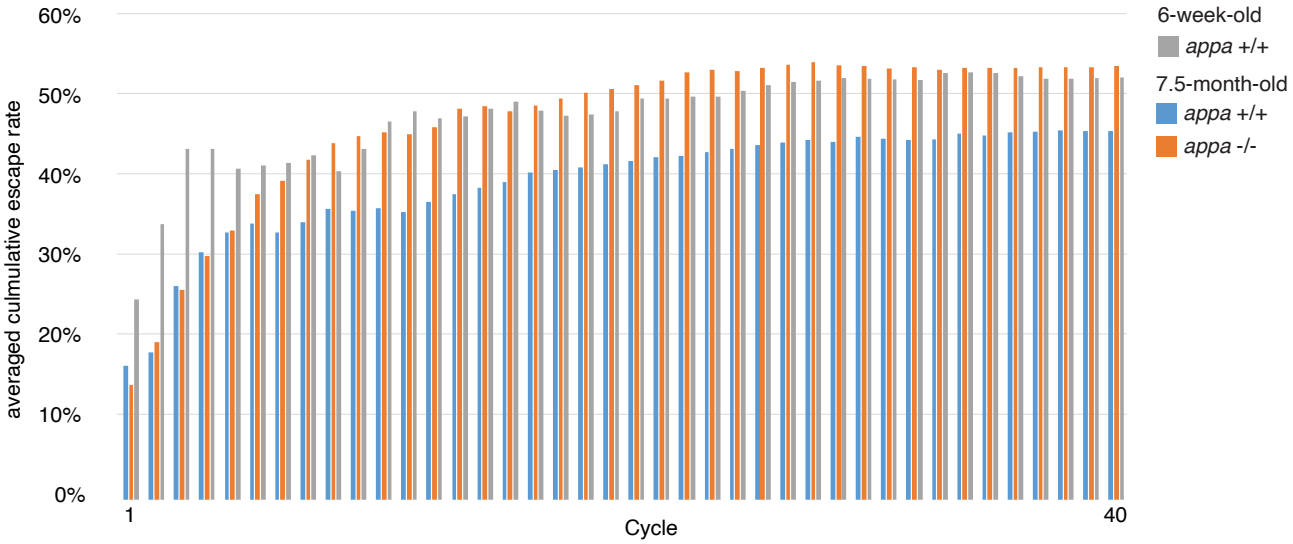

Figure S24. *appa* knock-out mitigates age-related learning deficiency in turquoise killifish. Plot describing the averaged cumulative escape rate of 7.5-month-old *appa* -/- mutants (orange, n = 28 fish) and their wild-type siblings (blue, n = 30 fish) across 40 cycles. In addition, a seperately conducted cohort of 6-week-old individuals has been tested and plotted (grey, n = 16 fish).